Spring 2016

Synthesis and functionalization of a triaryldiamine-base photoconductive/photorefractive composite, and its application to aberrated image restoration

Yichen Liang

Follow this and additional works at: https://scholarsmine.mst.edu/doctoral_dissertations

Part of the Chemistry Commons, and the Materials Science and Engineering Commons

Department: Chemistry

Recommended Citation

Liang, Yichen, "Synthesis and functionalization of a triaryldiamine-base photoconductive/photorefractive composite, and its application to aberrated image restoration" (2016). *Doctoral Dissertations*. 2482.
https://scholarsmine.mst.edu/doctoral_dissertations/2482

SYNTHESIS AND FUNCTIONALIZATION OF A TRIARYLDIAMINE-BASE PHOTOCONDUCTIVE/PHOTOREFRACTIVE COMPOSITE, AND ITS APPLICATION TO ABERRATED IMAGE RESTORATION

by

YICHEN LIANG

A DISSERTATION

Presented to the Faculty of the

MISSOURI UNIVERSITY OF SCIENCE AND TECHNOLOGY

In Partial Fulfillment of the Requirements for the Degree

DOCTOR OF PHILOSOPHY

in

CHEMISTRY

2016

Approved by

Dr. Jeffrey G. Winiarz, Advisor

Dr. Jie Gao

Dr. Yinfa Ma

Dr. V. Prakash Reddy

Dr. Jay A. Switzer

PUBLICATION DISSERTATION OPTION

This dissertation consists of the following four articles that have been published,

submitted, or prepared for publication as follows:

Pages 36-62 have been published in the Journal of Materials Chemistry C, 2015,

3, 4134.

Pages 63-84 have been prepared for the submission to the Journal of Organic

Electronics, 2016.

Pages 85–100 have been submitted to the Journal of Optics Letters, 2016.

ABSTRACT

Organic photorefractive (PR) composites have recently emerged as an important class of materials for applications including high-density data storage, optical communication, and biomedical imaging. In an effort to further improve their performance, this study focused on the utilization of functionalized semiconductor nanocrystals to photosensitize triaryamine (TPD)-based PR composites, as well as the application of TPD-based PR composites in the restoration of aberrated optical information. A novel approach to functionalize CdSe quantum dot (QCdSe) was firstly introduced where the sulfonated triarydiamine (STPD) was used as charge-transporting ligand to passivate QCdSe. TPD-based photoconductive and PR composites were photosensitized with the STPD-passivated QCdSe (SQCdSe). Due to the charge-transporting capability of STPD, the composites photosensitized with STPD-capped QCdSe exhibited superior performance relative to composites employing more traditional photosensitizers (such as fullerene C_{60} and trioctylphosphine-capped QCdSe), with figures-of-merit including photoconductivities in excess of 60 pS/cm, two-beam coupling gain coefficients in excess of 110 cm^{-1}, and PR response time of less than 30 ms. In addition, the ability of TPD-based PR composites to correct aberrations associated with a laser beam was described. Here, a severely aberrated laser beam was able to be restored to a nearly unaberrated condition through the PR process, and the potential of this technique for practical applications was well explained. Based on the current experimental geometry, a PR response time of 0.5 s was observed, which is the fastest PR response time reported for a PR composite operating under experimental conditions designed for the correction of optical aberrations.

ACKNOWLEDGMENT

First and foremost, I wish to extend my deepest appreciation to my research advisor and mentor, Dr. Jeffrey Winiarz, who has provided endless guidance and encouragement for me in accomplishing my PhD training, who is always ready to back me up whenever I struggled, and who is the giant offering his shoulder to support me. Being his student is a truly bless in my life.

I wish to thank my godfather and internship mentor in Brewer Science Inc., Dr. Jinhua Dai, who has provided me enormous hands-on guidance on organic synthesis, and served as my role model of a great scientist.

I owe my earnest thanks to my parents and my wife, whose love are the strongest motivation for my career. My thanks also go to my friends and colleagues, especially Dr. Tyler Fear, Dr. Jong-sik Moon, Mr. Wei Wang, Dr. Ruipu Mu, Mr. Patric Luber, Ms. Sonia Franz, and Mr. Bowen Weston, whose assistance and discussion led to considerable improvement in the quality of my research work.

Last but not least, I want to thank my committee members, Dr. Jie Gao, Dr. Yinfa Ma, Dr. V. Prakash Reddy, and Dr. Jay A. Switzer, for spending valuable time in guiding me accomplishing my PhD research.

DEDICATION

Dedicated to my princess and angel,

Jieying Qian

TABLE OF CONTENTS

LIST OF ILLUSTRATIONS

PAPER I

PAPER II

LIST OF TABLES

1. INTRODUCTION

1.1 SEMICONDUCTOR NANOCRYSTALS

Semiconductor nanocrystals, often referred to as quantum dots (QDs), are nano-sized inorganic semiconductor crystals. Since their development in the 1980s, QDs have become some of the most widely researched materials.[15] Different from bulk inorganic semiconductors, QDs commonly consist of hundreds to several thousand atoms. The diameters of QDs typically range from 2 to 20 nm, smaller than the Bohr radius, which is commonly regarded as the size of the exciton in the particular type of bulk material.[16] Under such conditions, the electronic wavefunction is confined by the dimensions of the QD. This phenomenon is known as the quantum confinement effect and the effect becomes more pronounced as the diameter of the QD is reduced.[17] As a result, the optical and electronic properties of the QD become size dependent. More specifically, the change in band gap, ΔE, is dictated by the size of the QD as illustrated by the equation

$$\Delta E = E_{\text{gap}} + \frac{h^2}{8R^2}\left[\frac{1}{m_e{}^*} + \frac{1}{m_h{}^*}\right], \tag{1}$$

Where E_{gap} is the band gap of bulk materials, R is the radius of exciton, and $m_e{}^*$ and $m_h{}^*$ are the reduced masses of electrons and holes, respectively[18]. Evident from eq. 4, as the radius of semiconductor crystals approaches the Bohr radius for that particular material, the ΔE becomes inversely related to crystal size. As shown in Figure 1.1, the size-dependent ΔE of QDs is reflected in their size-dependent optical absorption and photo-luminescence (PL).
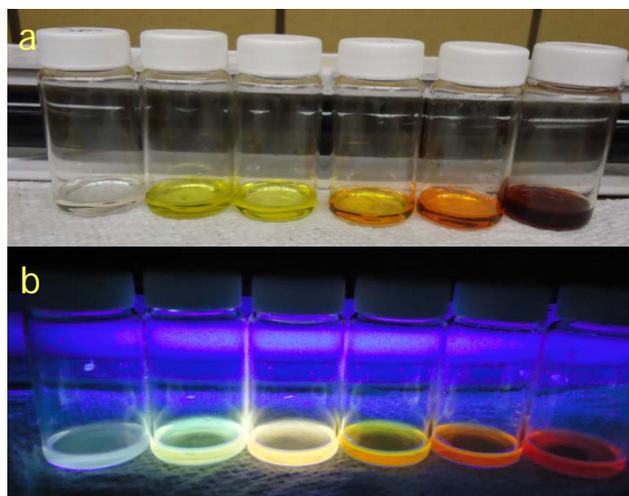
Figure1.1 CdSe QDs of different sizes (a) under ambient illumination, (b) under a UV lamp.

QDs can be synthesized via facile wet-chemistry techniques, where one of the precursors is dissolved a coordinating solvent and heated above the nucleation temperature, followed by a swift injection of the other precursor. During the synthesis, QDs are typically passivated with organic surfactants to retard aggregation and enhance solubility in certain solvents. The surfactants, in most cases, consist of a polar anchoring end group, such as thio-, amino-, carboxylic-, etc., which has an affinity for the surface of the QD. Since the size of QDs can be precisely controlled during synthesis by modifying the reaction conditions (duration, temperature, etc.) the optical and electronic properties of QDs can be conveniently manipulated.

Due to their unique properties, QDs have been successfully applied in the fabrication of various types of novel electro-optic devices including QD-based solar cells (QSC), QD-based light emitting diodes (QLED), QD-based lasers, etc. Research on QSCs started in the 1990s[19] and several significant breakthroughs have been made.

Efficiencies of ~ 7% have been reported which is competitive with traditional silicon-based solar cells.[19] Because the optical properties of QDs can be conveniently tuned by varying their size, the spectral characteristics of QSCs can be adjusted to coincide with the solar spectrum. Furthermore, quantum confinement enhances the extinction coefficient of QDs, leading to higher charge-generation quantum efficiencies.[20] In addition, QDs can be solvent-cast with various polymers in a thin film geometry, greatly reducing the cost of device fabrication when compared with silicon-based solar cells.[11] QLEDs are probably the most commercialized QD-based electronic devices currently in the market.[21] Due to the narrow emission band associated with monodisperse QDs, light emitted by QLEDs is more monochromatic than that of LEDs based in bulk materials. The tuning of the emission wavelength of OLEDs can also be accomplished by simply varying the size of the QDs. QD-based lasers is another field where QDs show significant potential for future large scale application.[22] Compared to traditional gas lasers or solid state lasers, QD-based lasers achieve broad coverage over UV and visible wavelength range. Additionally, QD-based lasers show a lower lasing threshold relative to commercialized quantum well lasers.[23] By changing the shape of QDs from spherical to rod-like, quantum rods can be used as special lasing materials which exhibit linearly polarized emission.[23]

QDs have also shown enormous potential in biological and medical imaging. For these applications, the fluorescent QDs are often tethered with bio-molecules, e.g. DNA, so that the bio-molecules can be traced with fluorescent microscopy.[24] Compared to traditional organic fluorescent dyes, QDs possess a higher quantum efficiency.[24] In

addition, the resistance of QDs to photo-bleaching endows them a longer lifetime than that of organic fluorescent dyes.[24]

1.2 PHOTOCONDUCTIVITY IN ORGANIC MATERIALS

Photoconductivity (PC) is a property of certain materials in which the electrical conductivity increases due to the absorption of photons resulting in an increase in the number of free charge-carriers.[1] During the PC process, the free charge-carriers, including both electrons and holes, are created through the excitation of electrons from the valence band, or the highest occupied molecular orbital (HOMO), to the conduction band, or the lowest unoccupied molecular orbital (LUMO) of the photoconductor (intrinsic photosensitization) or an added photosensitizer (extrinsic photosensitization). PC materials can be broadly categorized as inorganic or organic. Commonly used organic PC materials include phthalocyanines, squaraines, azo pigments, perylene pigments, and semiconductive polymers.[1] Extensively studied since the 1970s, organic PCs have found application in low-cost solar cells, xerography yielding more efficient photocopiers, photodetectors, light emitting diodes, and photorefractive (PR) devices. [2,3]

For the studies described herein, two types of organic photoconductors, poly(9-vinylcarbazole) (PVK) and *N,N'*-Bis(3-methylphenyl)-*N,N'*-diphenylbenzidine (TPD), have been employed and are depicted in Figure 1.2. PVK has been known as an efficient photoconductor since 1957, and has been used extensively in fields such as xerography.[1] PVK-based PR composites have exhibited outstanding performance, such as near 100% diffraction efficiencies[4] and millisecond response times, τ.[5] More recently, TPD and its derivatives have been used in PR composites[6] due to their relatively high charge-carrier

mobility (c.a. 100 times greater than that of PVK). Specifically, poly(acrylic tetraphenyldiaminobiphenol) (PATPD), a TPD-based polymer (see Figure 1.2), has been used in several PR composites exhibiting high figures-of-merit including a PC of ~1.5×10^4 pS/cm, a diffraction efficiency of 69%, and a $\tau = 8.71$ ms.[6] Additionally, because the ionization potential of PATPD is lower than that of PVK, an improvement in grating depth was observed.[6] In this work, monomeric TPD was used. The absolute positions of, and therefore the energy gap between, the HOMO and LUMO, E_g, are similar in TPD and PATPD, where TPD has $E_g = 3.20$ eV and PATPD exhibits $E_g = 3.23$ eV.[7,8] For this reason, their ionization potentials are also nearly equal, and therefore TPD and PATPD exhibit similar charge-transport properties in PR materials.
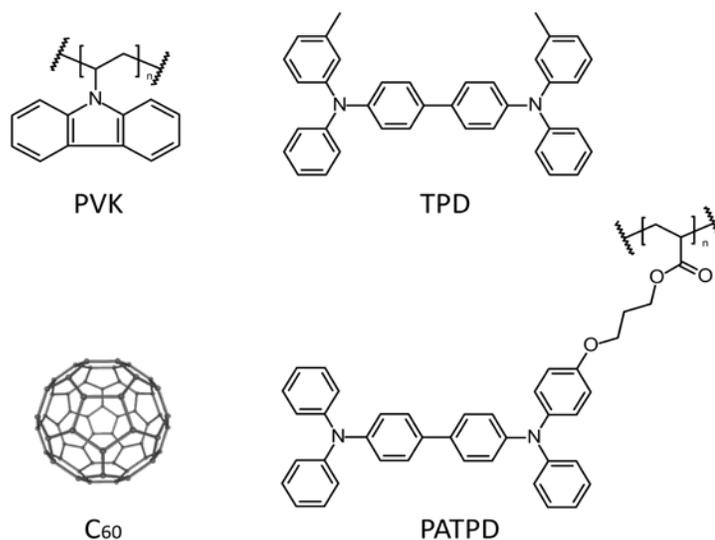
Figure 1.2 Molecular structure of PVK, TPD, C_{60}, and PATPD.

PVK and TPD are intrinsically PC for wavelengths shorter than ~400 nm,[9,7] and therefore an external photosensitizer must be doped into the composite for applications involving longer wavelengths. In this work, two types of photosensitizers have been

employed, fullerene C_{60} and semiconductor nanocrystals. C_{60}, with its molecular structure shown in Figure 1.2, has been known as one of the most efficient photosensitizers for PR composites because of its extraordinary electron accepting ability.[10] QDs, however show several potential advantages relative to C_{60}, including tunable operational wavelength[11] and facilitation of charge-carrier mobility.[12] A detailed discussion of the two types of photosensitizers can be found in Section 3.2.1.
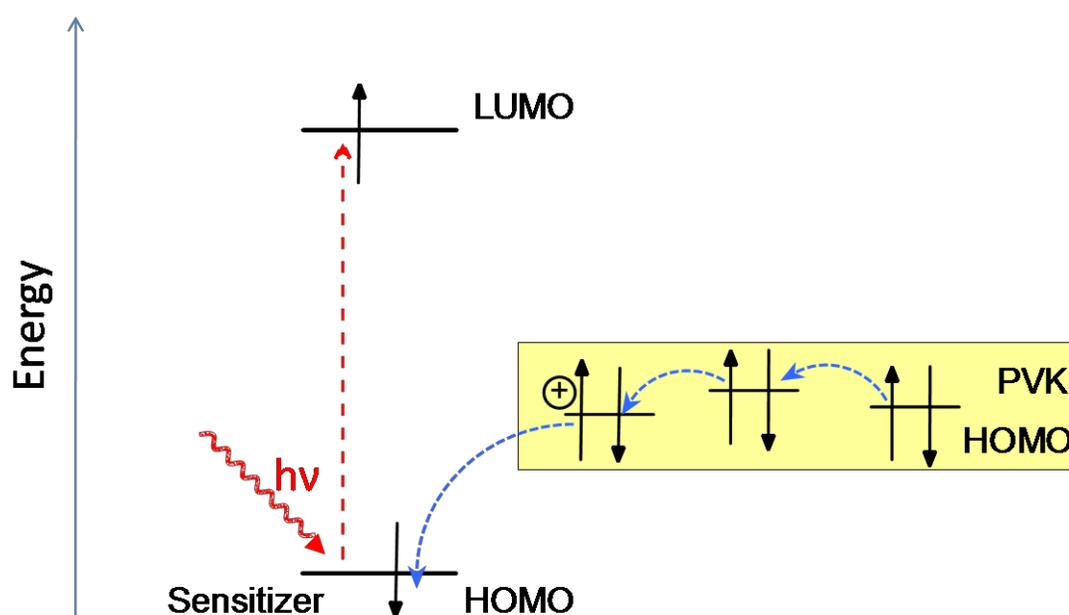
Figure 1.3 Energetics of PC in PVK- and TPD-based composites.

The mechanism of PC in PVK- and TPD-based composites can be explained in terms of the model shown in Figure 1.3. The process is initiated by the photo-excitation of the photosensitizer, generating holes and electrons in the photosensitizer's HOMO and LUMO, respectively. It is then energetically favorable for the PVK or TPD to reduce the photosensitizer, effectively injecting the hole into the HOMO of the charge-transport agent.[13] The holes can then migrate in the PC matrix under the influence of an externally

applied electric field, E. The migration involves the holes "hopping" between successive charge-transporting units (the carbazole groups in PVK and the arylamine functionalities in TPD). Based on this mechanism, only the holes are mobile in PVK or TPD, and the photo-generated electrons remain associated with the reduced photosensitizer until recombination occurs.[9]

The PC, σ_p, can be determined using the equation

$$\sigma_p = J_p/E \ , \tag{2}$$

where J_p is the photocurrent density. Similarly, the conductivity of the composite void of any illumination, known as the dark conductivity, σ_d, can be calculated using the equation

$$\sigma_d = J_d/E \ , \tag{3}$$

where J_d represents the dark-current density. J_p and J_d can be measured using a dc-photocurrent experiment, which is described in detail in Section 4.2. The PR performance of a composite is related to σ_p/σ_d.[50] Another parameter characterizing the performance of a photosensitizer is the photo-charge generation quantum efficiency, Φ, which is the ratio between the number of mobile charge-carriers, N_{cc}, and the number of absorbed photons, N_{ph}. Φ can be determined using the equation

$$\Phi = \frac{N_{cc}}{N_{ph}} = \frac{\sigma_p hcE}{Ie\lambda\alpha} \ , \tag{4}$$

where h is Planck's constant, c is the speed of light, I is the intensity of the incident light beam, e is the elementary charge, and α is the optical absorbance of the PC composite.[14]

1.3 PHOTOREFRACTIVITY IN ORGANIC MATERIALS

1.3.1 Background. The PR effect refers to the process in which the refractive index, n, of a material is spatially modulated in response to non-uniform illumination. Specifically, two coherent laser beams interfere in the PR material, resulting in regularly spaced regions of constructive and destructive interference within the material. This distribution in intensity induces an internal space-charge field, E_{sc}, formed by the photo-generation of free charge-carriers and their redistribution through the charge-transport process. The E_{sc} is then translated into a spatial modulation in the n through an electro-optical response with the magnitude of modulation directly related to the magnitude of the E_{sc}. Therefore, a phase grating is created in the material which can diffract incident light. A detailed description of the PR mechanism can be found in Section 3.2. The PR effect was first discovered in $LiNbO_3$ crystals in 1966[25] and initial PR research focused exclusively on inorganic crystals. Numerous PR crystals were discovered and studied thoroughly, such as KNbO3, $BaTiO_3$, and GaAs, and potential applications, such as holographic data storage and optical image processing, were proposed.[26,27] However, the fabrication of inorganic PR crystals is laborious and costly, and an expensive chamber is required.[25,26] In 1990, the PR effect was demonstrated in organics, specifically the organic electro-optical crystal, 2-cyclooctylamino-5-nitropyridine (COANP) doped with 7,7,8,8-tetracyanoquinodimethane (TCNP).[28] Although there were several drawbacks with the COANP/TCNP composite, such as low optical photosensitivity, inferior grating contrast, and phase separation between COANP and TCNP upon aging, the first organic PR material drew enormous attentions due to its low cost, ease of fabrication, and feasibility of controlling the operational properties through manipulation of the

constituents.[28] Motivated by this achievement, organic PR materials have been investigated extensively for the past two decades, and a variety of organic PR materials have been discovered exhibiting competitive or superior performance relative to their inorganic counterparts. Unlike the first PR organic crystal, today's organic PR materials are typically amorphous PR composites, fully-functionalized PR polymers, or polymer-dispersed liquid crystals.[13] The work described herein focuses on amorphous PR composites.

Generally, amorphous PR composites consist of a photosensitizer, charge-transport species, nonlinear optical (NLO) chromophore, and plasticizer. As described in Section 1, this study used C_{60} and/or QDs as the photosensitizers, and employed PVK and TPD as the charge-transport agents. The NLO chromophore refers to a type of molecule designed with an electron withdrawing group located at one end of the molecule and an electron donating group at the other end. Because of this structure, NLO chromophores have a strong ground-state dipole moment, and can interact with the E_{sc} to produce the modulation in n required in the PR process. The electro-optical response of the NLO chromophore is optimized when the glass transition temperature, T_g, of the composite is near or below the ambient operational temperature.[29] Hence, in most polymer-based composites, it is necessary to incorporate an external plasticizer to lower the T_g.

1.3.2 Mechanism. To effectively initiate the PR effect, optical intensities of several mW/cm^2 are typically required.[13,26] Various types of lasers, including Ar ion,[37] He-Ne,[38,39,40,42] and diode[43,44] lasers, have been used, with the most common being the He-Ne laser with λ = 633 nm. This is probably due to the relatively long coherent length (typically several tens of centimeters),[46] as well as their relatively low cost.
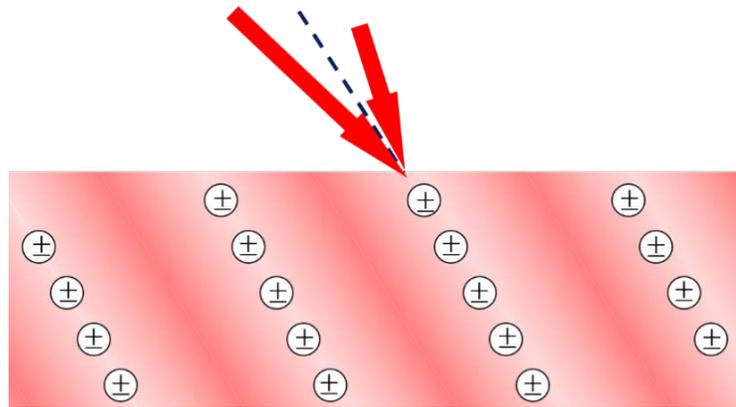
Figure 1.4. Photo-generation of charge-carriers.

1.3.2.1 Charge-carrier photo-generation. As depicted in Figure 1.4, non-uniform illumination is achieved through the interference of two coherent laser beams in the PR material. This initiates the photo-generation of charge-carriers, which involves the photo-excitation of the photosensitizer resulting in the creation and dissociation of electron-hole pairs. Under the influence of an external electric field, *E*, the electron-hole pairs, bound by a Coulombic force, can dissociate to create free electrons and holes. In most organic PR materials, holes are the mobile charge-carriers and may drift through the material under the influence of *E*, or alternatively recombine with its counter electron.[13,26] Hence, a competition exists between the photo-generation of holes and the recombination of holes with the counter electron. The result of this competition

influences the quantum efficiency, Φ, of the photo-generation process. In cases where recombination does not occur, the photo-generated electrons are trapped at the LUMO of the photosensitizer, forming anion radicals.[30] The character of the anion radicals have a strong impact on the growth of the PR grating because the anion radicals can act as trapping sites for mobile holes.

The photosensitizers used in organic PR composites can be broadly classified as three major types: organic π-conjugated molecules, QDs, and metal complexes. Because C_{60} and QDs are the photosensitizers used in this study, the discussion here is limited to organic π-conjugated molecules and QDs. The fullerenes and fluorenone-based molecules constitute the most commonly used organic π-conjugated photosensitizers with C_{60} being the most widely used in the visible due to its high Φ at these wavelengths. A direct correlation has been demonstrated between the high Φ of C_{60} and its strong electron accepting capability.[31] While aggregation of C_{60} in organic matrices frequently occurs at concentrations $> \sim 1$ wt.%,[26,32] the fluorinone-based molecules exhibit better compatibility with most PR matrices due to their aryl-based molecular structure.[33,34] Commonly used fluorinone-based PR photosensitizers include 2,4,7-trinitro-9-fluorenone (TNF) and (2,4,7-trinitro-9-fluorenylidene) malononitrile (TNFM) as depicted in Figure 1.5. The spectral characteristics of PR composites may correlate directly with the intrinsic absorption of the photosensitizer, or may reflect the formation of a charge-transfer complex between the photosensitizer and the charge-transporting species. For example, in PVK-based composites photosensitized with C_{60}, optical absorption primarily originates in the singlet state charge-transfer complex formed between PVK and C_{60}.[31] The spectral response of the various organic photosensitizers

covers the range of visible and near-infrared wavelength up to ~830 nm.[13] Several attempts have been made to extend this spectral response to the telecommunication wavelengths, i.e. 1310 and 1550 nm. For instance, 2-[2-{5-[4-(di-*n*-butylamino) phenyl]-2,4-pentadienylidene}-1,1-dioxido-1-benzothien-3(*2H*)-ylidene]malononitrile (DBM) (shown in Figure 1.5) was used to photosensitize PVK-based composites at 1550 nm through a two-photon absorption process.[35] Modified carbon nanotubes were employed as the photosensitizer at 1550 nm in a PVK-based composite.[36] However, in most instances the results were disappointing in that the diffraction efficiencies were lower than 5% and the PR τ were extremely slow.
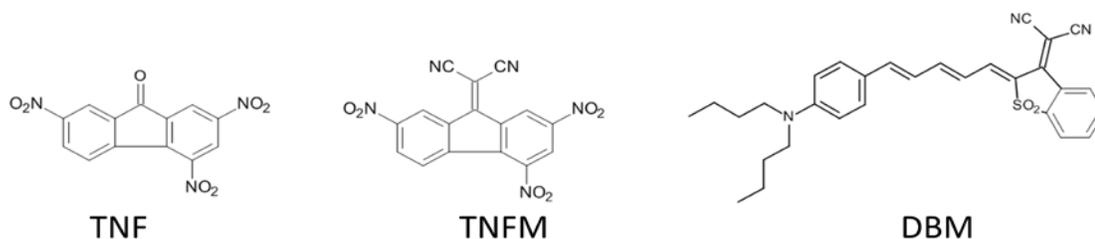
Figure 1.5 Molecular structure of TNF, TNFM, and DBM.

Due to the rapid advancement in nanotechnology, the photosensitization of PR composites with QDs has recently been realized.[13,26] QDs are especially appealing for this application due to their tunable spectral response, achieved through manipulation of their size and chemical composition. The first QD used in the photosensitization of PR composites was nanosized-CdS (QCdS), which showed PC performance competitive to similar composites photosensitized by C_{60}.[37] Inspired by this achievement, QDs with a variety of other compositions including CdSe,[38] CdTe,[39] NiS,[40] PbS,[41,42] PbSe,[43] and HgS[44] have been used as photosensitizers in PR composites. Table 1 provides a list of

their physical properties and performance. In an effort to photosensitize PR composites at the technically important telecommunication wavelengths of λ = 1310, 1550 nm, narrow band-gap QDs including PbS, PbSe, and HgS have been incorporated into the composites as photosensitizers.[41,43,44] Both of PbS and PbSe exhibited encouraging performance, with PbS-photosensitized composites showing Γ = 184.5 cm^{-1} at 1340 nm,[41] and PbSe-photosensitized composites demonstrating Γ = 86 cm^{-1} and η_{ext} = 40% at 1550 nm.[43] The performance of HgS-photosensitized composites were relatively disappointing with Γ = 4 cm^{-1} due to a low Φ.[44]

Another benefit of using QDs in organic composites is that the charge-transport process can be facilitated by the QDs. In a previous study, PVK doped with 7 wt% of QCdS experienced a three-fold increase in charge-carrier mobility.[12] This increase was attributed to the participation of QDs, which possess a higher charge-carrier mobility than the organics, in the charge-transport process.[12]

During synthesis, QDs are usually capped by a layer of surfactant molecules, e.g. oleic acid, or p-thiocresol, to prevent aggregation of the QDs. Unless intentionally removed (which, unless special precautions are taken, results in the rapid aggregation of the QDs), this surfactant layer remains associated with the QD into the PR composite. In many cases, these surfactants are electrically insulative, acting as a barrier to the charge-transfer process between the QD and the charge-transport matrix. Numerous attempts have been made to overcome this barrier. One of the most common approaches involves the post-synthesis exchange of the surfactant for ligands which are more conducive to the charge-transfer process, such as pyridene[39,40] and p-thiocresol.[37] This approach has

been found to greatly enhance the Φ. Unfortunately, the original, insulative surfactant is often not fully replaced by the substitute ligand and instability of the QDs often occurs after the ligand exchange. Another approach involves in-situ synthesis of the QDs in the PR composite void of any capping ligand. Specifically, in the case of QPbS, lead acetate was homogenously doped in the organic PR matrix, followed by exposure of the solid PR film to H_2S, forming QPbS in the matrix.[44] Although QPbS and QHgS have been successfully synthesized using this method, the composites photosensitized with them exhibited disappointing PR performance due largely aggregations and inhomogeneous size distribution of the QDs.[44] More recently, a novel strategy has emerged where ligands conducive to the charge-transfer process are used directly in the synthesis of the QDs instead of the traditional insulative ligands.[45] Here, sulfonated PVK (SPVK) was employed as the capping ligand in the synthesis of QCdSe, which was subsequently used as the photosensitizer in PVK-based PR composites. The PR composites devised using this approach showed a higher charge-generation efficiency than did simply blending 4-methylbenzenethiol-capped QCdSe with the organic matrix, and a two-fold increase in the two-beam coupling coefficient, Γ, was observed.[45] Inspired by these results, the work herein describes using sulfonated TPD (STPD) as the charge-transfer ligand in the synthesis of QCdSe. Due to the sulfonate group, STPD has a strong affinity for the surface of inorganic QCdSe. The STPD-capped QDs exhibited an extraordinary ability to photosensitize TPD-based composites, showing a 15-fold improvement in photoconductivity relative to composites sensitized with the more traditionally used trioctylphosphine oxide (TOPO)-capped QCdSe. Moreover, the PR composites

photosensitized with STPD-capped QCdSe showed $\Gamma = 120$ cm^{-1}, a 30% improvement

over the composites photosensitized with TOPO-capped QCdSe.

Table 1.1 Physical properties and photosensitizing performance of QDs used as photosensitizers for organic PR composites

Type	Particle Size/nm	Capping Ligands	Operational wavelength/nm
CdS	1.6~1.8	*p*-thiocresol	515
CdSe	6.2	Oleic acid	633
CdTe	4.0	Pyridene	633
NiS	5.9~14.4	Pyridene	633
PbS	6.0~8.0	Oleic acid	1340
PbSe	5.0	Oleic acid	1550
HgS	10.0	None	1300

Type	Photoconductivity/(S/m)	Two-beam Coupling Gain Coefficient, Γ (cm^{-1})[b]	External Diffraction Efficiency η_{ext} (%)[b]
CdS	7.9×10^{-9}	59.5	8.0
CdSe	N/A[a]	N/A[a].	20.0
CdTe	8.0×10^{-10}	39.0	24.0
NiS	N/A[a]	79.0	40.0
PbS	N/A	184.5	N/A[a]
PbSe	3.8×10^{-6}	86.0	40.0
HgS	N/A[a]	4.0	N/A[a]

a. Not provided in literature; b. Definition of two-beam coupling gain coefficient and external diffraction efficiency can be found in Section 4.3 and 4.4.

1.3.2.2 Space-charge Field. Following the photo-generation of charge-carriers, a E_{sc} is established through the transport and subsequent trapping of the holes, while the electrons remain associated with the photosensitizer. The holes are associated with the HOMO of the organic photoconductor, which is energetically dispersive compared with the highly ordered conduction band of inorganic crystals.[13,26] Due to this dispersive nature, a relatively large E is typically employed, and drift, rather than diffusion, is the dominant charge-transport process. According to the Gaussian-Disorder-Model, the drift of holes in organic photoconductors can be viewed as a process in which the charge-carriers "hop" between respective charge-transport units, e.g. the carbazole group of PVK, under the influence of E.[13] Additionally, the transport of holes in organic photoconductors is highly dependent on E and temperature, as implied by the equation

$$\mu = a_0 \rho \exp\left(-\frac{2\rho}{\rho_0}\right) \exp\left(\frac{-\Delta}{kT}\right) \exp\left[\beta\sqrt{E}\left(\frac{1}{kT} - \frac{1}{kT_0}\right)\right], \tag{5}$$

where μ is the mobility of charge carriers, a_0 is a constant specific to the material, β and T_0 are parameters fit to the experimental data, ρ is the mean distance between dopant molecules, k is Boltzmann's constant, ρ_0 is the wave function decay length, and Δ is the zero-electric field activation energy.[47]

The mobile charge-carriers can be trapped at trapping sites which can be internal and external. Internal trapping sites usually refer to charge-transport units which, due to the environment of the functional unit, are lower in potential energy and are typically

shallow in nature.[13] Internally trapped charges may be thermally detrapped. External

trapping sites are primarily attributed to the photosensitizer and NLO chromophore

included in the PR composite. The anion radicals of photosensitizers created during

photo-charge generation can act as recombination sites for mobile holes. If the HOMO

level of NLO chromophore is higher than that of the charge-transport molecule, the

chromophore can also serve as a trapping site for mobile holes. External traps typically

constitute deep traps and detrapping can be difficult. Deep traps should be avoided in the

design of PR composites, as previous investigations indicate an inverse relation between

the concentration of deep traps and charge-carrier mobility.[48]

As mentioned in Section 3.2.1, an alternating light intensity pattern is created in

the PR composite as the first step in the PR process. In the bright regions, the rate of

charge-carrier generation exceeds that of trapping, while in the dark regions, only

trapping of charge-carriers can occur.[49] As a result of the generation, transport and

trapping processes, charge-carriers are redistributed such that there is an accumulation of

positive charges in the dark regions and negative charge in the bright regions, forming an

E_{sc} as illustrated in Figure 1.6.[49] The magnitude of the E_{sc} can be described using the

equation

$$E_{SC} = mE_q[1 + (\frac{\sigma_d}{\sigma_p})]^{-1}[\frac{E_0^2 + E_d^2}{E_0^2 + (E_d^2 + E_q^2)}],$$ (6)

where m is the depth of modulation, E_0 is the component of E coincident with the grating

vector, and E_q and E_d are the magnitudes of the trap-density-limited space-charge field

and the diffusion field, respectively.[50]
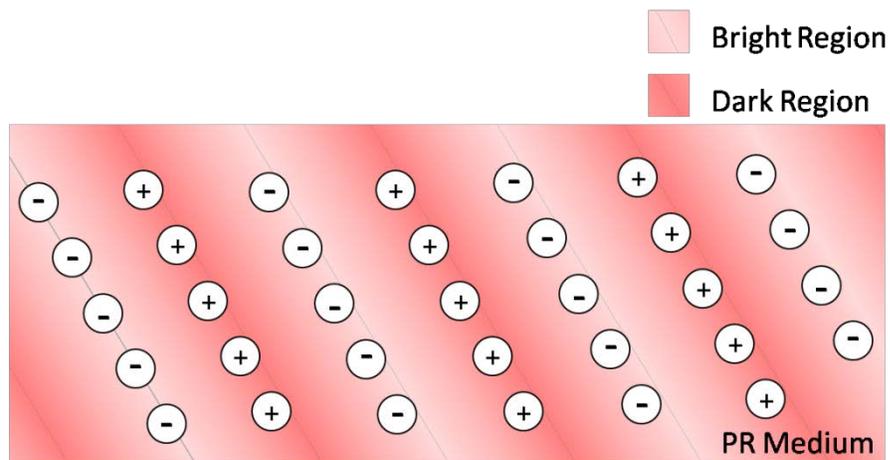
Figure 1.6 Formation of the E_{sc} in a PR medium.
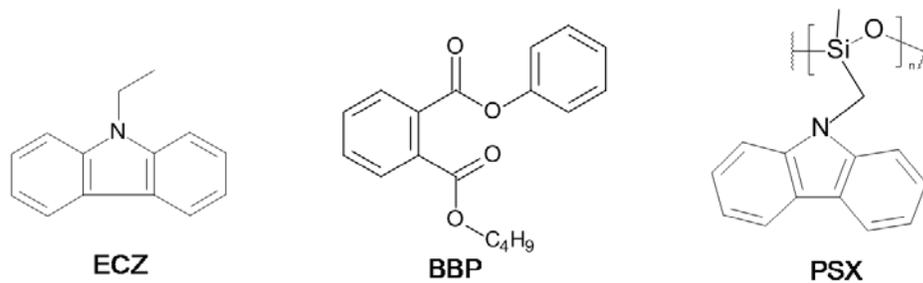
Figure 1.7. Molecular structure of ECZ, BBP, and PSX.

The charge-transport material plays a critical role in the formation of the E_{sc}.

Typical charge-transport materials used in organic PR composites are hole-conducting

polymers with funtional units, e.g. carbazole, and triphenyl diamine, on their main- or

side-chains with the concentration in the composite ranging from 40% to 70%. In the 1990s, PVK was the mostly widely used charge-transport material in PR composites due to its outstanding PC performance.[51] The carbazole groups on the side-chain of PVK serves as the charge transport unit. Several milestones were achieved using PVK-based PR composites, such as the first net optical gain[52] and near 100% internal diffraction efficiency.[53] Because the T_g of PVK is typically above 200 °C, the inclusion of an external plasticizer is necessary for the NLO chromophore to have sufficient orientation mobility to be poled by the E_{sc}.[29] Commonly used plasticizers includes *N*-ethylcarbazole[39,40] (ECZ) and butyl benzyl phthalate (BBP) [54] with their molecular structures illustrated in Figure 1.7. To avoid the inclusion of plasticizers, poly[methyl-3-(9-carbazolyl)propylsiloxane] (PSX) with $T_g \approx 50$ °C, was developed.[55] As shown in Figure 1.7, the low T_g of PSX stems from the large bond length and bond angle of the Si-O bonds in the polysiloxane backbone. PSX-based composites exhibit PR performances comparable to that of the PVK-based systems.[55]

Despite the success of PVK-based PR composites, the relatively low charge-carrier mobility, $\mu \approx 10^{-7}$ - 10^{-6} cm^2/Vs at $E = 40$ - 60 V/μm,[56] limits their dynamic performance. Experimental evidence indicates a direct correlation between the μ of the hole-transport species and the τ of the PR composite.[13] Therefore, recent research has focused on the replacement of carbazole-based hole conductors with TPD-based hole conductors, which exhibit a μ approximately two orders of magnitude greater than that of PVK. Attributed to the higher μ, TPD-based PR composites have been known to exhibit $\tau < 1$ ms,[6,7] considered as the fastest τ so far among organic PR materials. The

disadvantage of using TPD-based composites is that they have a relatively low density of internal charge-traps, which may lead to a diminished E_{sc} lowering the diffraction efficiency.[57]

1.3.2.3 Modulation of refractive index. The final step of the PR process is the translation of the E_{sc} into a modulation in the n and is accomplished through the inclusion of the NLO chromophore. Two mechanisms, the Pockels effect and the orientational birefringent effect, may lead to this modulation in n. The Pockels effect stems from the second order nonlinear electronic polarizability of a molecule which causes the n of the molecule to be dependent on the applied electric field according to the equation

$$\Delta n_{\mathrm{p}} = -\frac{n^3 r_{\mathrm{eff}} E_n}{2}, \tag{7}$$

where Δn_{p} is the magnitude of modulation in n, r_{eff} is the effective electro-optic coefficient, and E_{n} is the magnitude of the effective local electric field.[51] The Pockels effect is associated with NLO chromophores which exhibit a high hyperpolarizability.[13,26,51] The orientational birefringent effect may be significant in PR composites provided the T_{g} of the composite is below the operational temperature.[29] As illustrated in Figure 1.8, in such a composite, the highly dipolar NLO chromophores have sufficient mobility to be poled by the local electric field.[13,29] Because the NLO chromophores are electrically anisotropic, the effective n of NLO chromophores depends on their orientation relative to the direction of the incident beam. Because the orientation of the NLO chromophores will modulate across the PR device, corresponding to the modulation associated with the E_{sc}, there will also exist a spatial modulation in n. It's

worth noting that the modulation in *n* is shifted relative to the light intensity pattern by $\pi/2$. This phase shift leads to an asymmetrical exchange in energy between the two writing beams, which is one of the most important distinguishing characteristics of a PR grating. PR gratings with such a phase shift are known as nonlocal gratings.
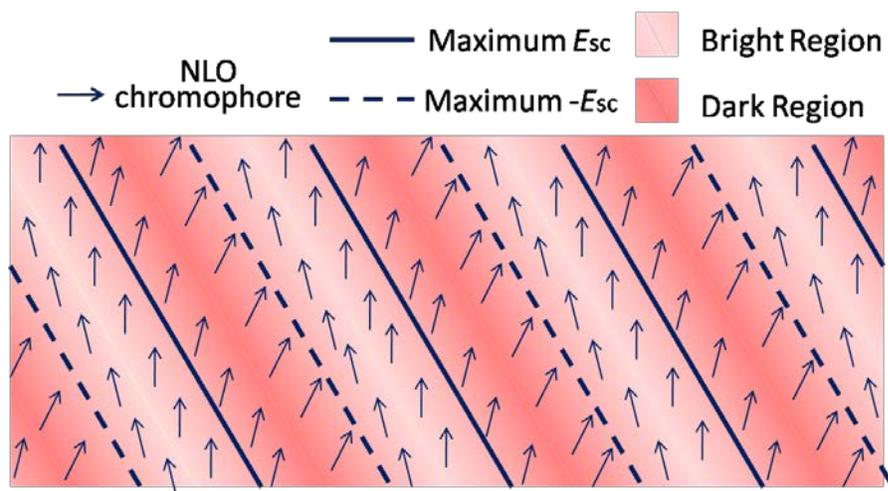
Figure 1.8 Birefringent modulation of refractive index.

Several aspects need to be considered when designing a NLO chromophore. First, a NLO chromophore should possess a high hyperpolarizability and electronic anisotropy in order to maximize Δn. This can be accomplished by modifying the electron withdrawing and donating groups. The three NLO chromophores used in this study include 4-azacycloheptylbenzylidene-malononitrile (7-DCST), benzylidenemalononitrile (AODCST), and diethylamino-nitrostyrene (DEANST) with their molecular structures shown in Figure 1.9. It is often desirable to maximize the loading of NLO chromophores in a PR composite in an effort to maximize the Δn, however, these high concentrations can also result in phase separation between the chromophores and charge-transport matrix. Additionally, highly dipolar molecules, such as the NLO chromophores used in

these composites, can also be detrimental to the charge-transport process.[58] Typical

chromophore concentrations in PR composites range from 30% to 50%. Furthermore, the

electronic energy levels of the chromophores, especially the HOMO, should complement

that of the charge-transport species. If the HOMO of chromophore is sufficiently higher

in energy than that of the charge-transport species, the chromophore may act as a deep

trap.[59]
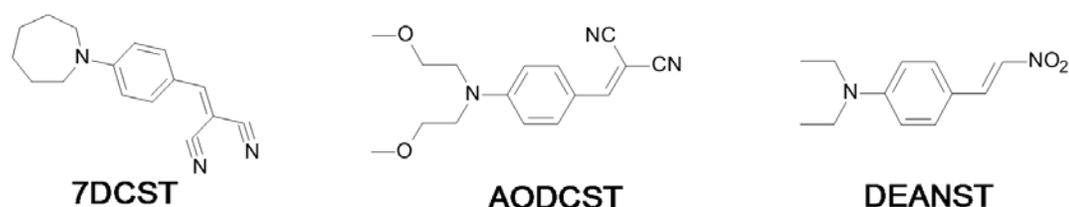
Figure 1.9 Molecular structure of DEANST, 7DCST and AODCST.

1.4 EXPERIMENTAL TECHNIQUES

The experimental techniques including device fabrication and material

performance testing are introduced in this section. The PR devices were fabricated using

the so-called "sandwich" technique, in which the active polymeric layer is covered by

two pieces of indium-tin-oxide coated glasses. The performance tests include

photoconductivity measurement, two-beam coupling and degenerated four-wave mixing

experiments.

1.4.1 Fabrication of PR Composites. In this study, PR devices were fabricated

using the "melt-pressing" technique.[13] Here, the components were co-dissolved in a

suitable solvent, typically toluene or chloroform, filtered using #5 filter paper to remove

any undissolved solids, followed by evaporation of the solvent in a vacuum oven at

temperatures below 50 °C. The dry solids were collected and melted on a hot plate at > 200 °C. The liquefied solids were further homogenized using a surgical blade and subsequently sandwiched between two pieces of ITO coated glass slides, which serve as transparent electrodes. The thickness of the active layer ranged from 50 to 100 μm in this study and was controlled using micro-sized glass beads. Figure 1.10 shows the fabricated PR devices.

Figure 1.10 Examples of PR devices used in this study.
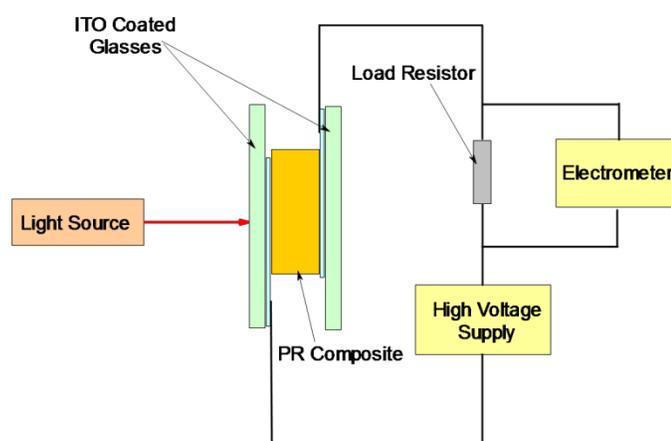
Figure 1.11 Experimental geometry used in photoconductivity characterizations.

1.4.2 Photoconductivity Characterization. The σ_p of the PR devices were characterized using a dc-photocurrent technique with the experimental geometry shown

in Figure 1.11. The photocurrent could be measured as a function of E using a Keithley electrometer. PR devices were subject to pre-illumination and a steady state was achieved prior to measurement. Dark conductivities, σ_d, were also determined using the geometry shown in Figure 1.12. σ_d and σ_d can be calculated using eqs. 2 and 3 as shown in Section 2.
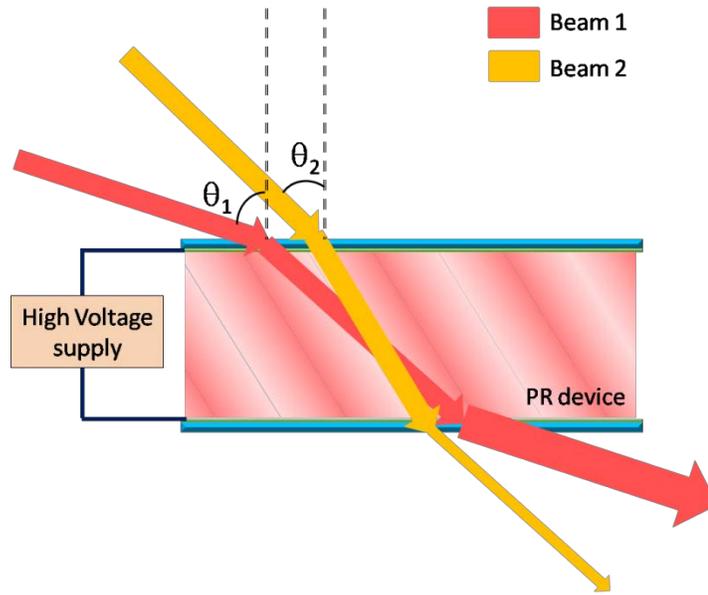
Figure 1.12. TBC experimental geometry.

1.4.3 Two-beam Coupling. Two-beam coupling (TBC) experiments were conducted using the geometry illustrated in Figure 1.12. Two coherent beams with p-polarization were incident at the PR device at angles of θ_1 = 30 - 45° and θ_2 = 60 - 75° relative to the normal of PR device surface.[26] The PR device was biased by an E of typically 30 – 100 V/μm. Rooted in the $\pi/2$ phase shift between the illumination pattern and modulation in n, asymmetrical energy transfer occurs between beam 1 and 2, and the direction of energy transfer can be alternated by changing the direction of E. Here, beam

1 is assumed to be the beam experiencing gain. The degree of this coupling can be represented by Γ, which can be calculated using the equation

$$\Gamma = [\ln(\gamma\beta) - \ln(\beta + 1 - \gamma)]/L , \tag{8}$$

where β is the ratio of the intensities of beam 1 and 2, γ is the ratio of intensities of beam 1 with and without beam 2, and L is the path length of beam 1 in the PR medium.[13,26] L can be calculated using the eq.

$$L = d/\cos\theta_1 , \tag{9}$$

where d is the thickness of the PR film.
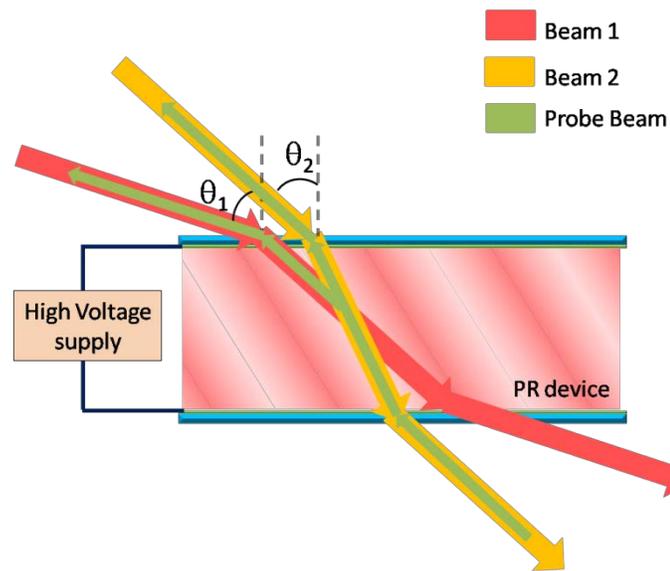
Figure 1.13 DFWM experimental geometry.

1.4.4 Degenerate Four-wave Mixing. The experimental geometry used in degenerate four-wave mixing (DFWM) characterizations is quite similar to that of TBC. As shown in Figure 1.13, coherent beams 1 and 2 are responsible for writing the PR

grating in the device, while a probe beam counter propagates to one of the writing beams. Here, the probe beam is assumed to counter propagate to beam 2. A portion of the probe beam is diffracted by the PR grating written by beams 1 and 2. The internal and external diffraction efficiencies of the PR gratings, η_{int} and η_{ext}, respectively, are defined by the equations

$$\eta_{\text{int}} = \frac{I_{\text{d}}}{I_{\text{d}}+I_{\text{t}}}, \tag{10}$$

$$\eta_{\text{ext}} = \frac{I_{\text{d}}}{I_{\text{p}}}, \tag{11}$$

where I_{d} is the intensity of the diffracted probe beam, I_{t} is the intensity of the transmitted portion of the probe beam, and I_{p} is the intensity of probe beam before passing through the PR device.[13,26]

To avoid any interference with the PR grating, the probe beam is made to be much weaker than the writing beams, and the polarization of the probe beam is orthogonal to the polarization of writing beams. Due to the geometry of the PR grating, a *p*-polarized beam experiences a larger diffraction efficiency than would an *s*-polarized beam.[60] Therefore, to optimize the experimental results, the writing beams are commonly *s*-polarized while the probe beam is *p*-polarized.

Time-resolved DFWM can be conducted by measuring the intensity of the diffracted probe beam as a function of time, and the results can be used to study the dynamics of the PR grating. For instance, the growth rate of PR grating can be determined by fitting the data of the time-resolved DFWM experiment to the equation

$$\eta(\text{t}) = E_{\text{sc}}[1 - \exp(-t/\tau_{\text{g}})], \tag{12}$$

where $\eta(\text{t})$ is the time dependent internal diffraction efficiency.[61]

1.5 APPLICATION OF ORGANIC PR MATERIALS IN THE CORRECTION OF AN ABERRATED LASER BEAM

The transmission of a noise-free signal is a critical requirement in optical comminication.[62] Unfortunately, aberrations introduced by the transmission media, e.g. optical fiber, atmosphere, etc, are almost unavoidable, and degrade the quality of the transmitted optical signal. To remove these aberrations, traditional approaches involve the application of adaptive optics, in which the wavefront aberration is reduced through the deformation of a mirror such that the aberrations can be compensated.[62,63] More recently, holographic techniques, especially those involving the PR effect, have been proposed for this application.[61,64,65] This novel approach has many advantages including low cost and ease of operation.[61,64,65] The first proof-of-concept experiment was conducted based on a DFWM geometry as illustrated in Figure 1.14.[64] Here, an s-polarized object beam, B1, with phase U_{obj} traversed an aberrator, which introduced an aberrated phase, $e^{i\varphi}$, into B1, resulting in an aberrated B1 with the phase $U_{\text{obj}}e^{i\varphi}$. An unaberrated reference beam, B2, with s-polarization interfered with B1 and wrote a volume holography in a PATPD-based PR composite. An unaberrated probe beam, B3, with a p-polarization counter propagated to B2, producing B4 with a phase of $U_{\text{obj}}^{*}e^{-i\varphi}$ (U_{obj}^{*} is the phase conjugate of U_{obj}), the phase conjugate of the aberrated B1. When B4 passed through the aberrator, a phase aberration, $e^{i\varphi}$, was introduced and effectively canceled its intrinsic aberration, $e^{-i\varphi}$, forming an aberration-free object beam counter

propagating to its original direction. Although this approach was effective in the restoration of an aberrated beam, it has an apparent drawback in that the information coming from the sender was finally redirected back to the sender with no net information being sent to a receiver.[61]
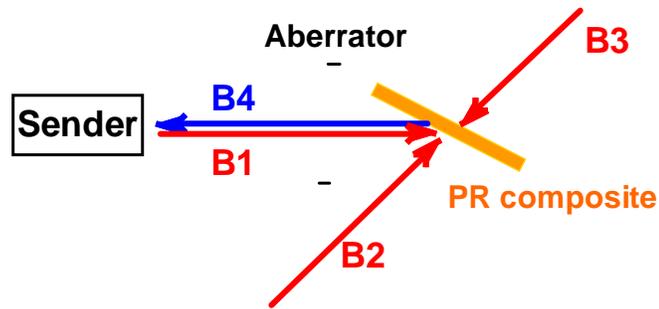
Figure 1.14 Conventional DFWM geometry for the elimination of phase aberrations based on the PR process.

To address this disadvantage, a novel system was introduced based on a forward DFWM geometry, as illustrated in Figure 1.15.[61] Here, the optical information was carried by B1 which contained both *s*- and *p*-polarization. B1 traversed the aberrator and its phase was aberrated as $e^{i\varphi}$. The unaberrated reference beam, B2, which was *s*-polarized, overlapped with B1 in a PVK-based PR composite, writing a PR grating by interfering with the *s*-polarized portion of B1. Because the aberrated phase, $e^{i\varphi}$, was introduced to B1 before traversing the PR composite, the aberration was written into the PR grating and the beams diffracted by the PR grating were subject to a phase aberration of $e^{-i\varphi}$. Therefore, when the *s*-polarized B1 was diffracted by the PR grating, the intrinsic aberration of B1, $e^{i\varphi}$ canceled the aberration introduced by the PR grating, $e^{-i\varphi}$, producing an unaberrated B3, which contained all the information associated with B1. As evident in Figure 1.15, a sender and a receiver can be clearly identified in this geometry and the experimental results demonstrated that a large portion of the aberrations could be

corrected. Nevertheless, this approach requires B2 to be unaberrated and coherent with B1, which is impractical for real applications. Additionally, the growth rate of the PR grating was relatively low with a response time of 9.3 s.[61] In an effort to address these disadvantages, an improved optical system is proposed and detailed in Paper III.
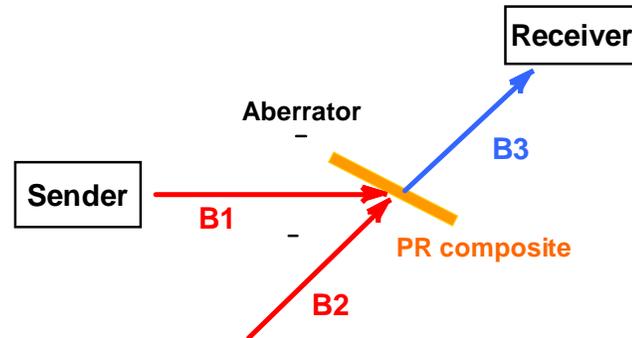
Figure 1.15 Forward DFWM geometry for the ellimination of phase aberrations based on the PR process.

REFERENCES

1. K. Law, *Chem. Rev.*, **1993**, 93, 449.

2. L. Zhang, T. Yang, L. Shen, Y. Fang, L. Dang, N. Zhou, X. Guo, Z. Hong, Y. Yang, H. Wu, J. Huang and Y. Liang, *Adv. Matter.*, **2015**, 27, 6496.

3. A. Dodabalapur, *Solid State Commun*. **1997**, 102, 259.

4. K. Meerholz, B. L. Volodin, B. Kippelen and N. Peyghambarian, *Nature*, **1994**, 371, 497.

5. D. Wright, M. A. Díaz-García, J. D. Casperson, M. DeClue, W. E. Moerner and R. J. Twieg, *Appl. Phys. Lett.* **1998** , 73 , 1490.

6. J. Thomas, R. A. Norwood, N. Peyghambarian, *J. Mater. Chem.* **2009**, 19, 7476.

7. J. Thomas, C. Fuentes-Hernandez, M. Yamamoto, K. Camnack, K. Matsumoto, G. Walker, S. Barlow, B. Kippelen, G. Meredith, S. Marder, and N. Peyghambarian, *Adv. Mater.* **16**, 2032 (2004).

8. P. K. Nayak, N. Agarwal, N. Periasamy, M. P. Patankar and K. L. Narasimhan, *Synth. Met.*, **2010**, 160, 722.

9. H. Block, S. M. Bowker and S. M. Walker, *Polymer*, **1978**, 19, 531.

10. S. Kober, F. Gallego-Gomez, M. Salvador, F. B. Kooistra, J. C. Hummelen, K. Aleman, S. Mansurova and K. Meerholz, *J. Mater. Chem.*, **2010**, 20, 6170.

11. D. V. Talapin, J. Lee, M. V. Kovalenko and E. V. Shevchenko, *Chem. Rev.*, **2010**, 110, 389.

12. J. G. Winiarz, L. Zhang, M. Lal, C. S. Friend and P. N. Prasad, *Chemical Physics*, **1999**, 245, 417.

13. S. Kober, M. Salvador and K. Meerholz, *Adv. Matter.*, **2011**, 23, 4725.

14. J. Moon, Y. Liang, T. E. Stevens, T. C. Monson, D. L. Huber, B. D. Mahala and J. Winiarz, *J. Phys. Chem. C*, **2015**, 119, 13827.

15. Z. Zhang, C. Wang, R. Zakaria and J. Y. Ying, *J. Phys. Chem. B.* **1998,** *102,* 10871.

16. G. R. Meseck, R. Kontic, G. R. Patzke and S. Seeger, *Adv. Funct. Mater.* **2012**, *22*, 4433.

17. Y. Bai, H. Yu, Z. Li, R. Amal, G. Q. Lu and L. Wang, *Adv. Mater.* **2012**, *24*, 5850.

18. T. Kippeny, L. Swafford and S. Rosenthal, *J. Chem. Educ.* **2002**, 79, 1094.

19. Q. Saquib, A. Al-Khedhairy, M. A. Siddiqui, F. M. Abou-Tarboush, A. Azam and J. Musarrat, *Toxicology in Vitro,* **2012**, 26, 351.

20. S. V. Voitekhovich, D. V. Talapin, C. Klinke, A. Kornowski and H. Weller, *Chem. Mater.* **2008**, 20, 4545.

21. J. M. Caruge, J. E. Halpert, V. Wood, V. Bulovic and M. G. Bawendi, *Nature*, **2008**, 2, 247.

22. S. Barillet, A. Simon-Deckers, N. Herlin-Boime, M. Mayne-L'Hermite, C. Reynaud, D. Cassio, B. Gouget and M. Carriere. *J. Nanopart. Res.*, **2010**, 12:61, 73.

23. L. Li, M. Sillanp, M. Tuominen, K. Lounatmaa and E. Schultz. *Ecotox. Environ. Safe.* **2013**, 88, 89.

24. A. M. Garcia, M. S. Fernandes and P. J. Coutinho. *Nanoscale Res. Lett.* **2011**, 6, 426.

25. A. Ashkin, G. D. Boyd, J. M. Dziedic, R. G. Smith, A. A. Ballmann, H. J. Levinstein and K. Nassau, *Appl. Phys. Lett.* **1966**, *9*, 72.

26. O. Ostroverkhova and W. E. Moerner, *Chem. Rev.* **2004**, 104, 3267.

27. A. E. T. Chiou and P. Yeh, *Opt*. *Lett*., **1985**, 10, 621.

28. K. Sutter and P. Gunter, *J*. *Opt*. *Am*. *B-Opt*. *Phys*., **1990**, 7, 2274.

29. W. E. Moerner, S. M. Silence, F. Hache and G. C. Bjorklind, *J*. *Opt*. *Soc*. *Am*. *B*, **1994**, 11, 320.

30. E. Mecher, C. Brauchle, H. Horhold, J. C. Hummelen, K. Meerholz, *Phys*. *Chem*. *Chem*. *Phys*.**1999**, 1, 1749.

31. W. Ying and A. Suna, *J*. *Phys*. *Chem*. *B*, **1997**, 101, 5627.

32. S. Kober, F. Gallego-Gomez, M. Salvador, F. B. Kooistra, J. C. Hummelen, K. Aleman, S. Mansurova and K. Meerholz, *J*. *Mater*. *Chem*. **2010**, 20, 6170.

33. E. Sliwinska, S. Mansurova, U. Hartwig, K. Buse and K. Meerholz, *Appl*. *Phys*. *B*, **2009**, *95*, 519.

34. O. Ostroverkhova, D. Wright, U. Gubler, W. E. Moerner, M. He, A. Sastre-Santos and R. J. Twieg, *Adv*. *Funct*. *Mater*. **2002**, 12, 621.

35. S. Tay, J. Thomas, M. Eralp, G. Li, B. Kippelen, S.R. Marder, G. Meredith, A. Schulzgen and N. Peyghambarian, *Appl*. *Phys*. *Lett*. **2004**, 85, 4561.

36. A. D. Grishina, L. Y. Pereshivko, L. Licea-Jimenez, T. V. Krivenko, V. V. Savelev, R. W. Rychwalski and A. V. Vannikov, *High Energy Chem*., **2008**, 42, 378.

37. J. G. Winiarz, L. Zhang, M. Lal, C. S. Friend and P. N. Prasad, *J*. *Am*. *Chem*. *Soc*., **1999**, 121, 5287.

38. X. Li, J. V. Embden, J. W. M. Chon, R. A. Evans and M. Gu, *Appl*. *Phys*. *Lett*. **2010**, 96, 253302.

39. J. G. Winiarz, *J*. *Phys*. *Chem*. *C*, **2007**, 111, 1904.

40. T. M. Fears, C. Anderson and J. G. Winiarz, *J. Chem. Phys.*, **2008,** 129, 154704.

41. K. R. Choudhury, Y. Sahoo, S. Jang and P. N. Prasad, *Adv. Funct. Mater.*, **2005**, 15, 751.

42. J. Moon, Y. Liang, T. E. Stevens, T. C. Monson, D. L. Huber, B. D. Mahala and J. G. Winiarz, *J. Phys. Chem. C*, **2015**, 119, 13827.

43. K. R. Choudhury, Y. Sahoo and P. N. Prasad, *Adv. Mater.*, **2005**, 17, 2877.

44. J. G. Winiarz, L. Zhang, J. Park and P. N. Prasad, *J. Phys. Chem. B*. **2002**, 106, 967.

45. J. H. Park and O. Park, *Appl. Phys. Lett.*, **2006**, 89, 193101.

46. G. K. Ackermann, *Holography: A Practical Approach,* **2007**, Wiley-VCH.

47. J. X. Mack, L. B. Schein and A. Peled, *Phys. Rev. B*, **1989**, 39, 7500.

48. J. Oh, C. Lee, N. Kim, *J. Chem. Phys.*, **2009**, 130, 134909.

49. B. Kippelen, *Photorefractive Materials and Their Applications II:Materials*, *Springer Series In Optical*, **2006**, 487.

50. N. V. Kukhtarev, V. B. Markov, S. G. Odulov, M. S. Soskin and V. L. Vinetskii, *Ferroelectrics*, **1979**, 22, 949.

51. W. E. Moerner and S. M. Silence, *Chem. Rev.*, **1994**, 94, 127.

52. M. C. J. M. Doncker, S. M. Silence, C. A. Walsh, F. Hache, D. M. Burland, W. E. Moerner and R. J. Twieg, *Opt. Lett.*, **1993**, 18, 1044.

53. K. Meerholz, B. L. Volodin, B. Kippelen, N. Peyghambarian, *Nature*, **1994** , 371, 497.

54. N. Tsutsumi and W. Miyazaki, *J. Appl. Phys.*, **2009**, 106, 083113.

55. I. K. Moon, C. Choi and N. Kim, *J. Photochem. Photobiol. A: Chem.*, **2009**, 202, 57.

56. K. Ogino, T. Nomura, T. Shichi, S. Park, H. Sato, T. Aoyama and T. Wada, *Chem. Mater.*, **1997**, 9, 2768.

57. H. J. Bolink, C. Arts, V. V. Krasnikov, G. G. Malliaras and G. Hadziioannou, *Chem. Mater.*, **1997**, 9, 1407.

58. A. Goonesekera and S. Ducharme, *J. Appl. Phys.*, **1999**, 85, 6506.

59. O. Ostroverkhova and K. D. Singer, *J. Appl. Phys.*, **2002**, 92, 1727.

60. W. E. Moerner, A. GrunnetJepsen and C. L. Thompson, *Annu. Rev. Mater. Sci.*, **1997**, 27, 585.

61. J. G. Winiarz and F. Ghebremichael, *Appl. Opt.*, **2004**, 43, 3166.

62. S. Niu, J. Shen, C. Liang, Y. Zhang and B. Li, *Appl. Opt.*, **2011**, 50, 4365.

63. K. Baskaran, R. Rosen, P. Lewis, P. Unsbo and J. Gustafsson, *Optom. Vis. Sci.*, **2012**, 89, 1417.

64. G. Li, M. Eralp, J. Thomas, S. Tay, A. Schulzgen, R. A. Norwood, and N. Peyghambarian, *Appl. Phys. Lett.*, **2005**, 86, 161103.

65. J. Winiarz and F. Ghebremichael, *Opt. Express*, **2004**, 12, 2517.

PAPER

I. Functionalization of CdSe Semiconductor Nanocrystals With Organic Charge-Transporting Ligands

Yichen Liang, Jong-Sik Moon, Ruipu Mu and Jeffrey G. Winiarz

ABSTRACT: [1,1'-Biphenyl]-4,4'-diamine-N,N'-bis(3-methylphenyl)-N,N'-diphenyl (TPD), a well-studied hole transporting material, has been sulfonated using acetyl sulfate and subsequently used as a passivating ligand in the synthesis of CdSe quantum dots (QDs). It is further demonstrated that QDs synthesized through this approach are able to serve as efficient photosensitizers in photoconductive (PC) inorganic/organic hybrid composites. Fourier-transform infrared spectroscopy confirms that the sulfonate group has been bonded to the TPD molecule. UV/visible absorption and photoluminescence (PL) spectroscopy of the sulfonated TPD (STPD) indicate that sulfonation does not significantly alter the electronic properties of TPD. Furthermore, mass spectrometry shows STPD is primarily mono-sulfonated. The STPD capped CdSe QDs (STPD-QCdSe) clearly exhibit the effect of quantum confinement in their UV/visible absorption spectra. The PL spectra of STPD-QCdSe suggest the STPD is attached to the surface of QCdSe. The morphology of STPD-QCdSe has been studied using transmission electron

microscopy. The results indicate the STPD-QCdSe are approximately spherical with diameters of [3.1, 3.9] nm and highly crystalline. To demonstrate the enhancement in charge-transfer efficiency associated with STPD-QCdSe, two types of PC composites were fabricated. The first was photosensitized through the inclusion of STPD-QCdSe, and the other included CdSe QDs capped with trioctylphosphine (TOPO-QCdSe), with molecular TPD serving as the charge transport matrix in both cases. The PC was measured as a function of the external electric field, E, with the PC of the composite sensitized with STPD-QCdSe exceeding that of the composite sensitized with TOPO-QCdSe by a factor of ~15 with $E = 10$ V/μm.

Introduction

Semiconductor nanocrystals, also known as quantum dots (QDs) have aroused tremendous interest in fields concerning optical and electro-optic applications due to their unique properties (e.g. tunable absorption, narrow photoemission, etc).[1] Currently QDs have been successfully applied in the manufacturing of photodetectors,[2] solar cells,[3] light emitting diodes[4] and field effect transistors.[5] In the past several decades, there has been significant progress in the methods used in the synthesis of QDs with solution-based colloidal synthesis being one of the most commonly employed techniques.

Solution-based colloidal syntheses are relatively facile techniques that can produce QDs with controllable size and few crystalline defects. The QDs synthesized using these methods are often passivated with capping ligands consisting of an anchoring end group, e.g. thiol, amino-, carboxylic, etc., attached to a hydrocarbon chain. Due to the presence of hydrocarbon chain, these commonly employed ligands are electrically insulative in nature, thus hindering their use in applications relying on a charge-transfer process between the QDs and any conductive matrix in which the QDs are contained.[6,7] Different techniques have been investigated in an effort to eliminate the insulative layer, including the exchange of the long hydrocarbon capping ligands with smaller ligands (e.g. pyridine),[8] chemically removing the capping ligands by treating the QDs with sodium hydroxide[9] and gydrazine,[5] and heat annealing.[10] None of these techniques, however, can completely remove the insulating shell and, in most cases, the stability if the QDs is adversely affected. For these reasons it is desirable to synthesize the QDs directly in the presence of a passivating ligand which lends itself to the charge-transfer process.

The hole transporting material, [1,1'-Biphenyl]-4,4'-diamine-N,N'-bis(3-methylphenyl)-N,N'-diphenyl (TPD) is well-studied and has been widely used in both electronic and electro-optic devices.[11] Due to its π-stacking structure[12] and molecular conformation,[13] TPD exhibits a hole mobility of $\sim 10^{-3}$ cm^2/(Vs) under an externally

applied electric field, E, of below 1 V/μm,[12] an extremely high figure-of-merit among

organic hole transporting materials. However, due to its lack of appropriate functional

groups, it is unable to act as a passivating group in the synthesis of QDs. In this article, a

novel technique for the appropriate functionalization of TPD and the subsequent p

assivation of CdSe semiconductors nanocrystals (QCdSe) is reported. Here, the TPD was

modified through the covalent bonding of a sulfonate group to one of the phenyl groups

located on the TPD molecule resulting in sulfonated TPD (STPD), as illustrated in Fig 1.

Acetyl sulfate was selected as the sulfonation agent due to its relatively mild nature

compared with more typical sulfonating agents such as sulfuric acid, which may degrade

the TPD. Hence, whereas the pristine TPD lacks affinity for the surface of the QCdSe,

the functionalized TPD molecule readily associates with the surface of QCdSe due to the

presence of the electron-rich sulfonate group. The STPD was characterized using

UV/visible spectroscopy, photoluminescence (PL) spectroscopy, Fourier-transform

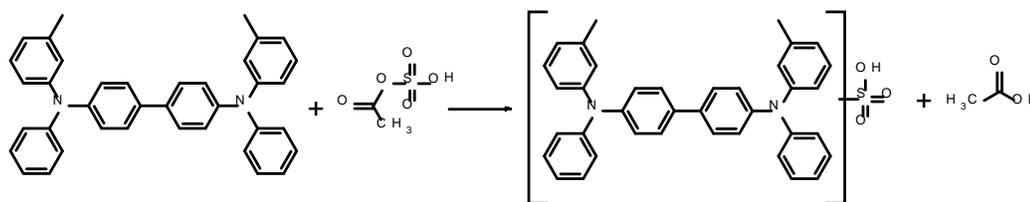infrared (FTIR) spectroscopy and mass spectrometry (MS).

Fig. 1 Sulfonation reaction for TPD.

The STPD was subsequently used as the surfactant/passivating ligand in the synthesis of QCdSe passivated with STPD ligands (STPD-QCdSe) in a facile, room temperature reaction, appropriately modified from that found in the literature.[14] The procedure on which this technique is based employed sulfonated polyvinyl carbazole (PVK) to synthesize QCdS.[14] Compared with PVK, TPD is reported to have higher charge drift mobility.[15] Hence, it is anticipated that TPD-based composites should demonstrate superior photoconductive (PC) properties. The STPD-QCdSe was characterized using UV/visible and PL spectroscopy, as well as transmittance electron microscopy (TEM).

PC experiments were conducted to evaluate any improvement in charge-transfer efficiency of STPD-QCdSe relative to that of QCdSe passivated with a more traditional passivating agent, trioctylphosphine (TOPO) in this case. Two types of PC samples were fabricated using TPD as the charge-transport matrix; one type photosensitized with STPD-QCdSe and the other type photosensitized with TOPO capped QCdSe (TOPO-QCdSe). The STPD-QCdSe and the TOPO-QCdSe were synthesized such that they possessed band-gap energies of similar magnitude, corresponding to a wavelength of $\lambda \approx$ 540nm. The PC experiments were conducted using Helium Neon laser operating at $\lambda =$ 543 nm.

Experiment

Chemicals

TPD was purchased from Magical Scientific Corporation. Cadmium acetate dihydrate, selenium powder (100 mesh, 99.99%), sodium borohydride (98%), acetic

anhydrate (99+%), 1-butanol (99.9%) and 1.2-dichlorobenzene (99% reagent plus) were purchased from Sigma Aldrich Corporation. Sulfuric acid (95%-98%) was purchased from Alfa Aesar Corporation. All chemicals were used as received. Deionized (DI) water was produced using an Advantage A 10 Mili-Q system from Millipore Corporation.

Sulfonation of TPD

The sulfonation agent, acetyl sulfate, was prepared based on a method described in literature[16] with minor modifications. Here, acetic anhydride (0.38 ml) was dissolved in 2 ml of chloroform and stored in an ice bath for 5 min after which 0.14 ml of 96% sulfuric acid was added dropwise. At temperatures lower than 10º C, acetyl sulfate is formed by the process illustrated in Fig. 2.[16] The final concentration of the prepared acetyl sulfate solution was 1 M and was used at this concentration in the subsequent sulfonation of TPD.
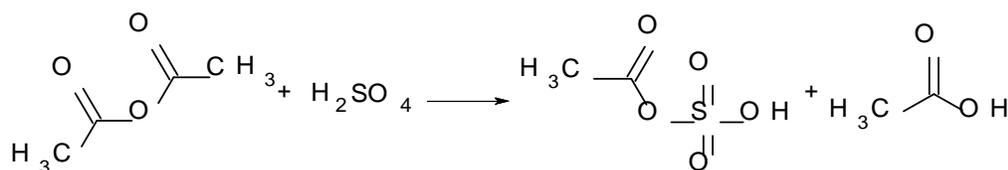
Fig. 2 The synthesis reaction of acetyl sulfate.

For the sulfonation of TPD, 50 mg of TPD was dissolved in a 20 ml glass vial containing 1 ml chloroform and placed in an ice bath. After 20 min, 150 μl of the prepared acetyl sulfate solution was added to the TPD/chloroform solution dropwise under strong magnetic stirring and the final mixture was placed in a temperature controlled vacuum oven with a temperature of ~ -5º C. The chloroform and acetic acid byproducts were removed gradually under vacuum. The removal of acetic acid shifted

the reaction toward the products, thus increasing the STPD yield. Upon removal of the solvent, the reaction vial was kept under vacuum for an additional 5 hr to remove residual acetic acid, finally yielding a light yellow powder. The reaction process is depicted in Fig. 1.

Characterization of STPD

Spectroscopic techniques including UV/visible spectroscopy, PL spectroscopy and FTIR spectroscopy as well as mass spectrometry were used to analyze both pristine TPD and STPD. The UV/visible spectroscopic characterization was conducted using a Cary 50 UV/visible spectrophotometer with TPD and STPD dissolved in a mixture of chloroform/butanol (3:1 by volume) at the same concentration of 0.01 mM. A quartz cuvette produced by Fisher Scientific Corporation was used as the sample cell.

PL characterization was conducted using a LS-5 Fluorescence Spectrophotometer produced by Perkin-Elmer Corporation. Samples were excited by a 330 nm light source. The same quartz cuvette used in the UV/visible spectroscopy was used in this PL spectroscopic analysis. The concentration of the analyte in each case was 0.01 M. No additional purification was conducted for the synthesized STPD prior to UV/visible or PL spectroscopic characterization.

For FTIR spectroscopic and mass spectrometric characterizations, STPD samples were purified by column chromatography using chloroform/methanol (2:1 by volume) as the elution phase. The FTIR spectra were taken using a Nexus 470 FT-IR spectrometer. The TPD and STPD samples used for FTIR were solvent cast on a sodium chloride pellet using chloroform/butanol (3:1 by volume).

Mass spectrometry measurements were conducted on an AB Sciex 4000 Q trap MS/MS system. The purified STPD samples were dissolved in methanol and injected into the spectrometer using the infusion technique. Negative mode was employed.

Synthesis of QCdSe using STPD Ligands

For the synthesis of STPD-QCdSe, 50 mg of TPD was sulfonated and used without additional purification. The STPD was dissolved in 4 ml chloroform/ethanol (1:1 by volume) forming a light-yellow solution. Sodium hydrogen selenide was prepared according to the steps described in literature[17] with minor modifications. Here, nitrogen gas was bubbled through 1.5 ml DI H_2O mixed with 1 ml ethanol under strong magnetic stirring for 5 min at room temperature to remove any dissolved oxygen. Subsequently, sodium borohydride (11.5 mg, 0.305 mmol) was dissolved into the solution. Selenium powder (11.5 mg, 0.145 mmol) was then added to the solution. A significant amount of foaming due to the evolution of H_2 was observed. The selenium powder was consumed within 10 min. The ensuing sodium hydrogen selenide stock solution was transparent and colorless and used for STPD-QCdSe synthesis without further processing. Different sized STPD-QCdSe were produced by varying the synthesis temperature. STPD-QCdSe labeled as 1, 2 and 3 were synthesized at temperatures of 20° C, 0° C and -15° C, respectively. For the synthesis, 75 μl of cadmium acetate dihydrate stock solution (0.02 mg/ml) was added to the STPD solution under magnetic stirring at room temperature. Subsequently, 110 μl of the prepared sodium hydrogen selenide stock solution was swiftly injected into the mixture. The reaction occurred almost immediately, as indicated by the lightening in the color of the mixture. Simultaneously, a red precipitate, later verified as STPD-QCdSe, appeared in the solution. The precipitate was separated from

the reaction mixture by centrifuging for 20 s. The liquid phase containing excess STPD was discarded and the precipitate was dispersed in 1 ml of 1,2-dichlorobenzene. To remove excess TPD, STPD, and STPD that may have been only loosely associated with the QCdSe cores, 0.5 ml of methanol was added to the STPD-QCdSe/dichlorobenze suspension precipitating the STPD-QCdSe. The solvent was discarded and the precipitated STPD-QCdSe was redispersed in dichlorobenzene. This precipitation/redispersion procedure was repeated three times. The STPD-QCdSe suspensions 1, 2, and 3 had dark red, red and orange color, respectively, with no visible scattering. QCdSe synthesized using this procedure, but without the addition of STPD, resulted in a brown product which could not be dispersed in any common solvent. This strongly indicates that the surfaces of the STPD-QCdSe are effectively passivated with the organic STPD ligands. The STPD-QCdSe/dichlorobenzene colloidal suspensions were stored for further characterization.

Nanocrystal Characterization

The synthesized STPD-QCdSe was characterized using UV/visible spectroscopy, PL spectroscopy and TEM. Spectroscopic characterizations were conducted on the same instruments used for STPD characterizations. For UV/visible spectroscopy, STPD-QCdSe with different particle sizes were dissolved in 1,2-dichlorobenze. For PL spectroscopy characterization, STPD-QCdSe3 was dissolved in 1,2-dichlorobenze. Similar concentrations of $\sim 5 \times 10^{-6}$ M were used in acquiring the UV/visible and PL spectra. As a comparison, the PL spectrum of STPD solution after adding cadmium acetate was also acquired. A Tecnai F20 STEM, operated at 200 kV, was used for TEM characterizations. To analyze its chemical composition, energy dispersive spectroscopy

(EDS) was also conducted on the STPD-QCdSe samples. The TEM sample was prepared by placing a drop of diluted dichlorobenzene dispersed STPD-QCdSe3 onto a 300 mesh copper grid. The copper grid, coated with a lacey carbon film, was purchased from Electron Microscopy Science Corporation.

Photoconductivity analysis

PC characterizations were conducted using a DC photocurrent technique where a Keithley electrometer was used to measure the current passing through the sample as a function of E. PC samples were fabricating by sandwiching the PC composite between two ITO coated glass plates with a thickness of 10 μm controlled by glass spacers. For this study, four PC composites were fabricated. Devices 1, 2 and 3 were photosensitized with STPD-QCdSe1, 2, and 3, respectively, and device 4 was photosensitized with TOPO-QCdSe. The concentrations of the photosensitizers were adjusted to achieve an absorbance of ~10 cm^{-1} at the excitation wavelength. The weight percentages of photosensitizers in devices 1 - 4 are 0.38 %, 0.39 %, 0.40 % and 0.40 %, respectively. All PC devices used TPD as the charge-transport matrix. The absorption spectra of devices 1 - 4 were acquired using the same spectrophotometer for STPD characterization. The PC experiments were conducted using helium-neon laser operating at the wavelength λ = 543 nm. The incident beam intensity is 2.31 mW. Both photoconductivity, σ_p, and dark conductivity, σ_d, were calculated using the equation $\sigma = J/E$, where J is the experimentally determined current density.

Results and discussion

Characterization of STPD

Fig. 3 illustrates the UV/visible absorption spectra of TPD, STPD and STPD-Cd conjugate (the result of reacting the STPD with the Cd precursor void of Se precursor), in chloroform/butanol (3:1 by volume). Evident in the figure, the absorption spectra of SPTD is very similar to that of pristine TPD. The greatest difference lies in the region from roughly 300 to 380 nm. Here, the shoulder seen in the TPD spectrum at ~320 nm becomes slightly less pronounced after sulfonation. Additionally, within the range of roughly 400 nm and 480 nm, there is a small increase in the absorption of STPD relative to that of TPD, which likely accounts for the light-yellow color of the STPD solution. Because the absorption peaks for TPD and STPD are at nearly the same position, it is likely that the band-gap was not significantly altered by the sulfonation process. The magnitudes of absorption for TPD and STPD at their respective maxima (~360 nm) were also comparable. These similarities indicate the sulfonation process did not significantly affect the electronic structure associated with TPD. With these results in mind, it is anticipated that the STPD will retain its potential for efficient charge transfer, integral to the intended application of passivating QCdSe for use as a photosensitizer in PC composites.

Fig. 4 illustrates the PL spectra of TPD and STPD. The PL peaks are located at approximately the same position (~430 nm). However, the PL quantum efficiency of STPD is reduced compared to that of TPD, indicating that the sulfonation process results in a non-radiative energy dissipation path in addition to the PL radiative process. Again,
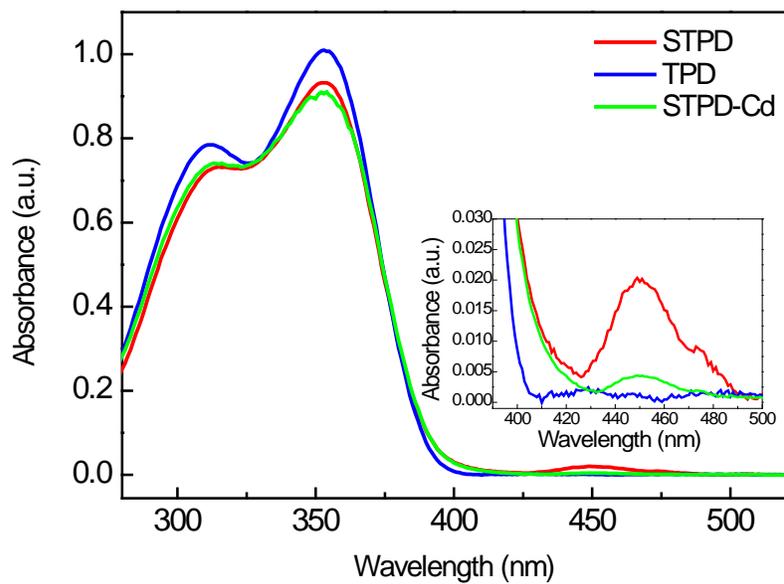
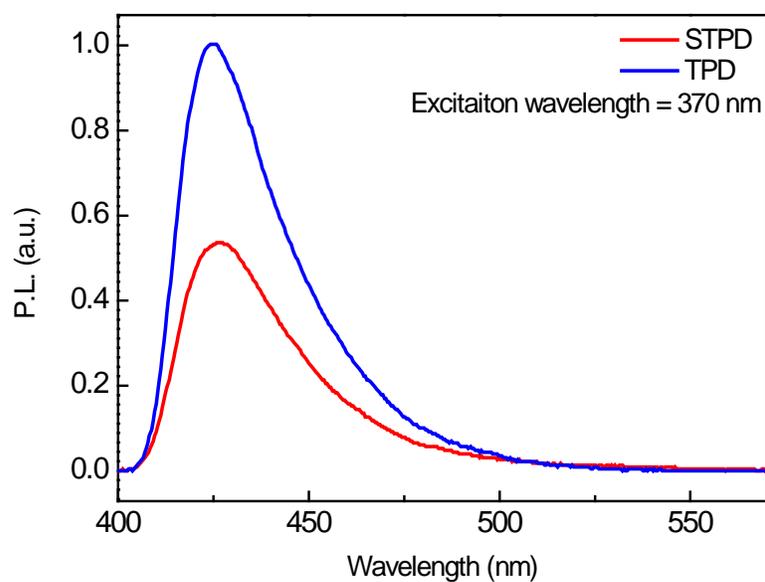**Fig. 3** UV/visible absorbance spectra of TPD and STPD

Fig. 4 PL spectra of TPD and STPD

the PL spectra imply that sulfonation did not significantly modify the electronic structure

of TPD.

FTIR spectroscopy was also used to characterize the STPD and the spectra of TPD and STPD are shown in Fig. 5. Compared to pristine TPD, the spectrum of STPD exhibits two additional peaks at 755 cm^{-1} and 1215 cm^{-1} which can be attributed to the S-O and S=O bond stretching vibrations, respectively.[18] With the exception of the newly observed peaks, no additional significant differences were identified. These data indicate that $-SO_3H$ has been successfully linked to the TPD molecule void of additional changes in the TPD structure.
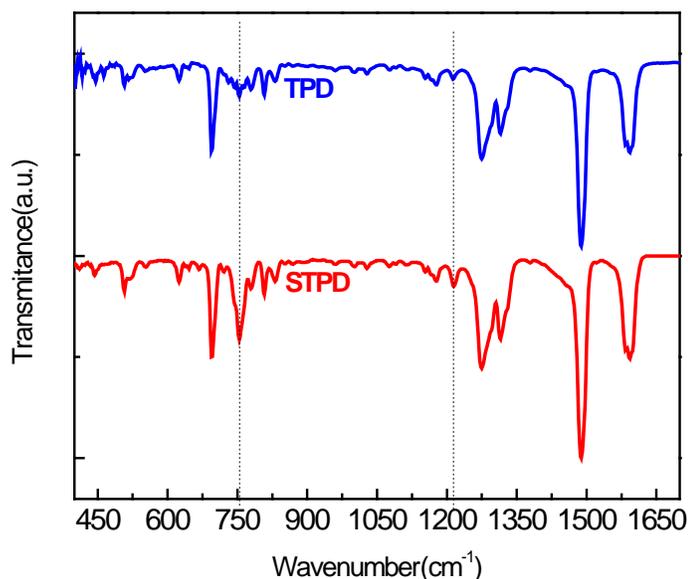
Fig. 5 FTIR spectra of TPD and STPD. The dashed lines designate the additional peaks attributed to the $-SO_3H$ group in STPD

Finally, MS spectrometry was used to characterize the synthesized STPD and is illustrated in Fig. 6. Only one intense peak at M/Z = 595, corresponding to mono-sulfonated STPD, is present in the spectrum. The reason for the mono-sulfonated TPD occurring as the major products is rationalized as follows. When the initial sulfonate group has bonded to the TPD molecule, the conjugated electrons associated with the

TPD molecule were shifted towards the electronegative sulfur atom in the sulfonate group, ultimately deactivating the TPD from any further reaction with the acetyl sulfate.
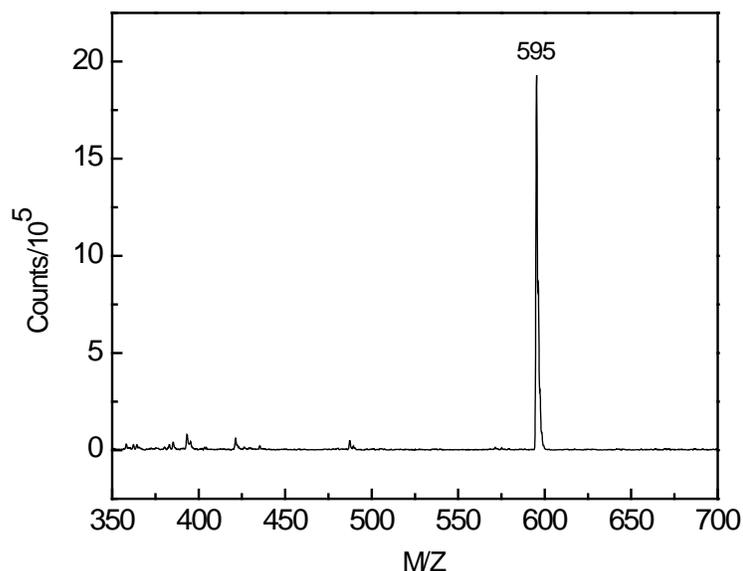
Fig. 6 Mass spectrum of STPD under negative mode.

Characterization of STPD-QCdSe

Fig. 7 illustrates the UV/visible absorption spectra of STPD-QCdSe. Because the STPD has no appreciable absorption in the range between 500 and 650 nm, the observed spectral features can be attributed to the CdSe component of the STPD-QCdSe. The band-gap of bulk CdSe is also indicated in the figure. In all three STPD-QCdSe, the location of the peak associated with the first exciton is blue-shifted relative to that of bulk CdSe, clearly showing the effects of quantum confinement. The spectra of STPD-QCdSe do not exhibit a sharp peak, but rather a relatively broad shoulder in the range from 500 nm to 600 nm. This feature indicates that the STPD-QCdSe have a broad particle size distribution, typical for QCdSe synthesized at low temperature.[19,20] For

applications requiring a relatively more narrow size distribution, size selective precipitation may be used to achieve a more mono-disperse product. Also evident is that as the temperature in the synthesis of the STPD-QCdSe is decreased, the peak is increasingly blue-shifted, indicating an associated decrease in particle size. The absorption shoulder of STPD-CdSe1 occurs at ~590 nm, while the absorption of STPD-CdSe2 and STPD-CdSe3 appear near ~570 nm and ~550 nm, respectively (see Fig 7). For comparison, bulk CdSe exhibits an absorption edge at approximately 712 nm at room temperature.

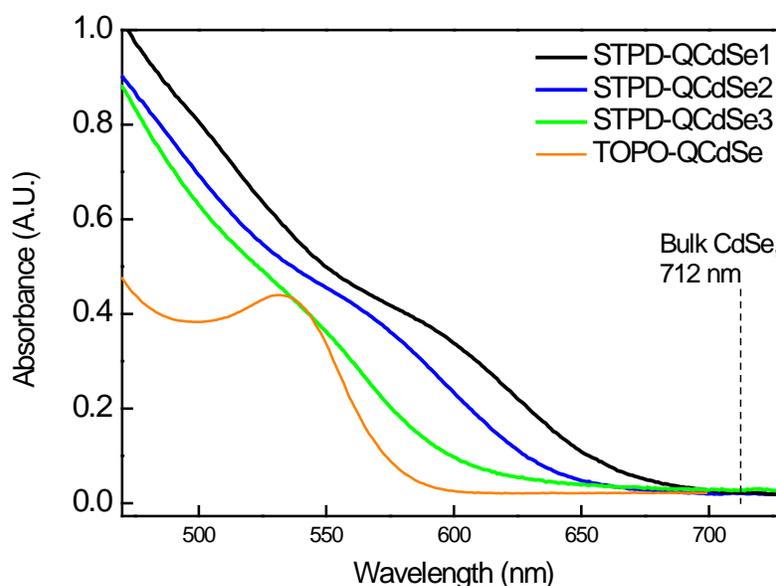
Fig. 7 UV/visible spectra of STPD-QCdSe1, 2 and 3, and TOPO-QCdSe

The normalized PL spectrum of STPD-QCdSe3 in 1,2-dichlorobenze is illustrated Fig. 8. For comparison, the PL spectra of STPD and STPD-Cd conjugate (the result of reacting the STPD with the Cd precursor void of Se precursor), both dissolved in chloroform/ethanol (1:1 by volume), were acquired as well. It is noted that the PL

spectrum of the STPD-Cd conjugate is slightly blue shifted relative to that of STPD, signalling the successful formation of the complex. This is also supported by the observed change in color associated with the addition of cadmium acetate to the STPD solution forming the STPD-Cd complex (see Fig. 3). In addition, the primary peak, associated with the STPD ligand is significantly broadened in the range of ~ 425 to 525 nm and there is also the emergence of a shoulder in the range of ~ 525 to 675 nm. The broadening of the primary peak attributed to the STPD ligand may be caused by several factors including steric effects caused by the crowding of the STPD on the QCdSe surface, which may lead to the deformation of the molecule, hence affecting the molecular energy levels. In addition, the bonding of the STPD ligand with QCdSe may shift the STPD energy levels accordingly. The emergence of the shoulder (~ 525 to 675 nm) is attributed directly to the QCdSe. It is assumed that this feature is in the form of a shoulder, and not a peak, due to the relatively broad size distribution associated with the QCdSe. The relatively low PL of the QCdSe can be attributed to the surface passivation with the charge transport ligands STPD. Here it is speculated that excited charge-carriers associated with the QCdSe can be transferred to the environment through the STPD ligands and subsequently trapped, rather than undergoing radiative recombination. This speculation is rationalized by consideration of the energy levels associated with TPD and CdSe, illustrated in Fig. 9.[21, 22, 23] While the quantum confinement effect can shift the positions of the valence band (VB) and conduction band (CB) in QCdSe, the relatively large particle size (>3 nm) of QCdSe investigated in this study indicates that the shift is less than 0.4 eV,[24] which can be neglected in the following comparison with TPD energy levels. As seen in the figure, it is energetically favourable for an electron which is photo-

excited to the CB of QCdSe to relax into the VB of TPD, thus hindering radiative recombination. The observed reduction in STPD-QCdSe thus indicates that the STPD ligands are conjugated on the surface of QCdSe nanocrystals. Similar PL quenching was also observed in QDs passivated with sulfonated PVK.[14] As illustrated in Fig. 8, the PL associated with the STPD ligand is largely retained in the PL spectrum of the STPD-QCdSe (in the range from 400 nm to 480 nm). During the synthesis procedure, excess STPD which was not tethered to the surface of QCdSe was removed during the washing process. It is further noted that the addition of methanol to a STPD/1,2-dichlorobenzene solution did not result in an observable precipitate, indicating that STPD remains soluble in this solvent combination and therefore excess STPD should be removed in the washing process. Therefore, the observed STPD emission in the PL spectrum of STPD-QCdSe3 can only be attributed to STPD associated with the surface of QCdSe. This also indicates that the surface of STPD-QCdSe has been successfully passivated with STPD.
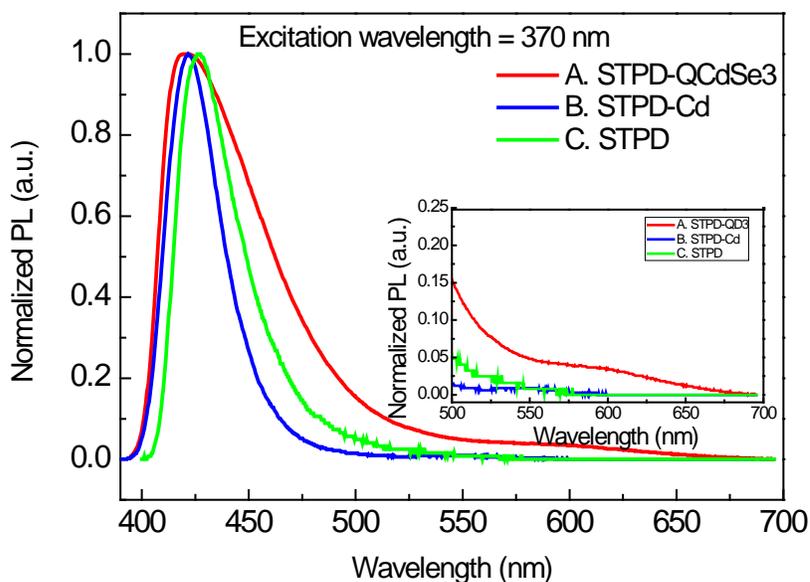

Fig. 8 PL spectra of STPD and STPD-QCdSe3
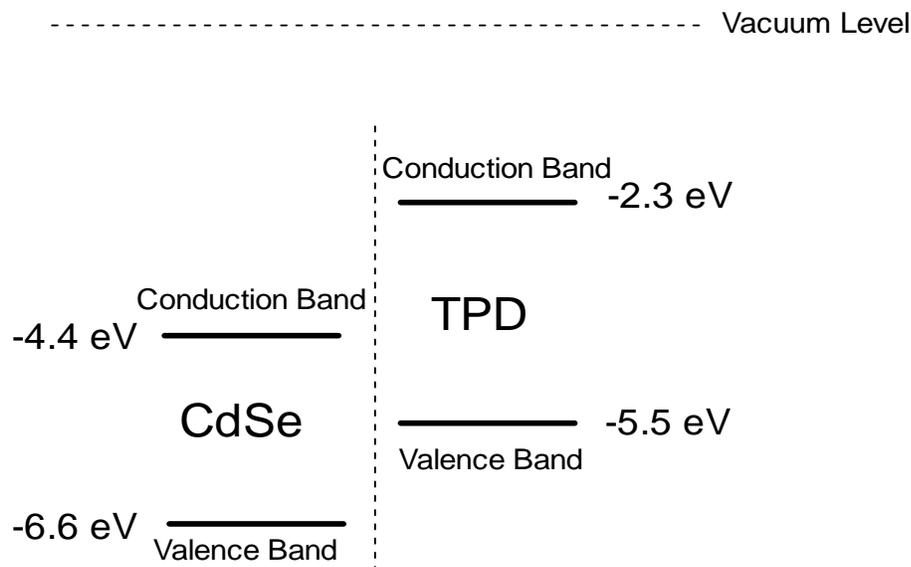
Fig. 9 VB and CB positions of TPD and CdSe.

The morphology of STPD-QCdSe3 was studied using TEM and the data are presented in Fig. 10. Evident from the figure, the QDs are roughly spherical in shape. The average particle diameter was 3.0 ± 0.5 nm ($n = 23$). Using 550 nm as the position of the absorption shoulder for STPD-QCdSe3 (see Figure 8), in conjunction with the empirical equation, $D = (1.6122 \times 10^{-9}) \lambda^4 - (2.6575 \times 10^{-6}) \lambda^3 + (1.6242 \times 10^{-3}) \lambda^2 - (0.4277) \lambda + 41.57$, where D (nm) is the diameter of QDs and λ (nm) is the absorption wavelength at the maximum,[25] the diameter of STPD-QCdSe3 was calculated to be 3.1 nm, consistent with the TEM data. By applying the same equation and using 590 nm and 570 nm as the position of absorption shoulder, the diameters of STPD-QCdSe1 and STPD-QCdSe2 were calculated as 3.9 nm and 3.5 nm, respectively. Based on the

experimental and calculated data, the radii of the synthesized QDs are smaller than the Bohr radius of CdSe of 5.6 nm,[26] resulting in the observed quantum confinement effect seen in Fig. 8. As seen in the TEM images, the STPD-QCdSe were evenly dispersed on the TEM grid, although a small amount of aggregation existed. The aggregation may suggest that the passivation of QCdSe using STPD is not as effective as with traditional ligands e.g. TOPO. The high-resolution TEM image also reveals that the QCdSe are well crystallized. The chemical composition of STPD-QCdSe3 is revealed in the EDS spectrum (Fig. 11). The peaks associated with Cd and Se elements evidently confirm the synthesized nanocrystals are CdSe. Quantified using the FEI TIA (TEM Imaging and Analysis) method, the molar ratio of Cd/Se is 55.33/44.55. The Peaks associated with Cu and C are representative of the carbon coated copper grid. The Cl-peak is attributed to residual solvent (dichlorobenzene). An S-peak exists in the spectrum which furthermore proves that STPD ligands were capped on the surface of CdSe nanocrystals.

For PC experiments, organic PC composites were fabricated using TPD as the charge-transfer matrix, while STPD-QCdSe1, 2 and 3 and TOPO-QCdSe were employed as photo-sensitizers. The TOPO-QCdSe were synthesized via a routine procedure,[6] with its absorption spectrum depicted in Fig. 7. The concentrations of the two types of photo-
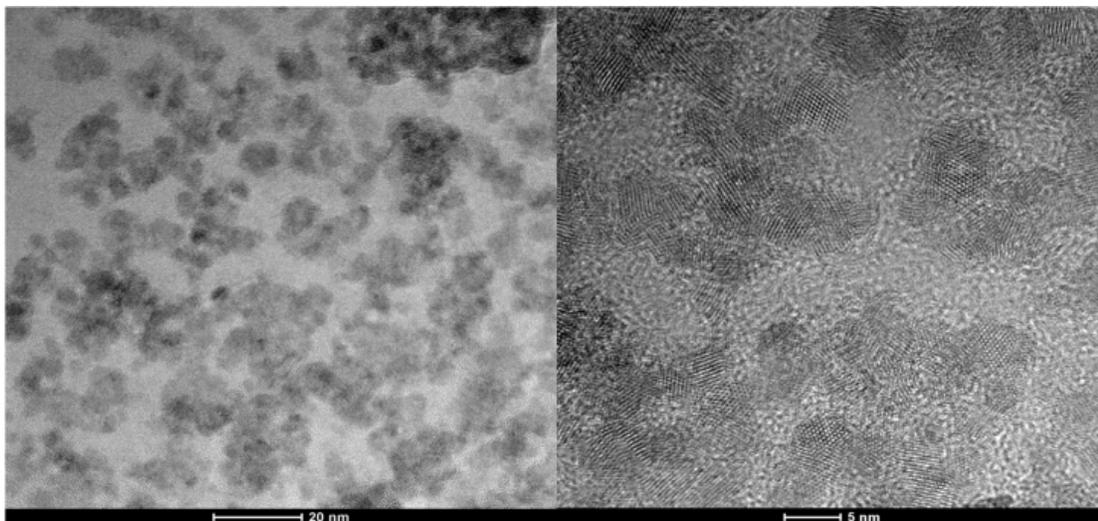
Fig. 10 TEM images of STPD-QCdSe3.
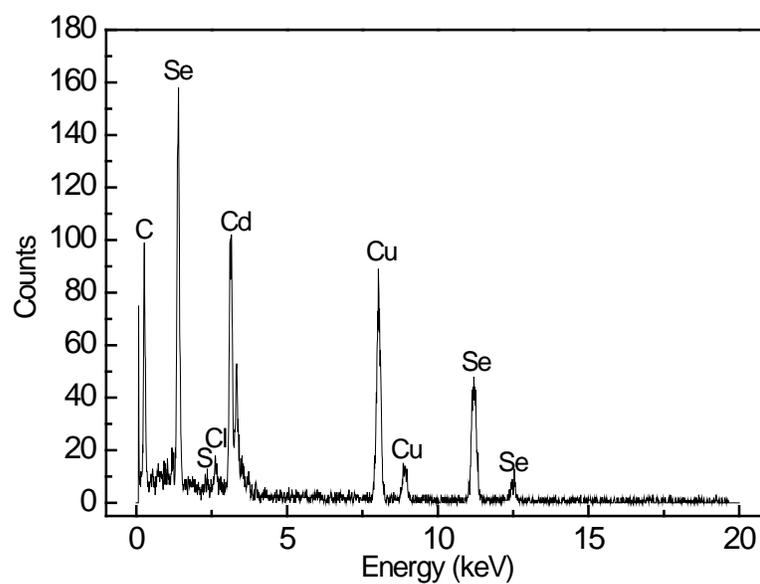
Fig. 11 EDS of STPD-QCdSe3.

sensitizers were tailored in order to ensure the composites have a similar absorption cross-section at 543 nm, the wavelength of the excitation source. The absorption spectra of the PC devices are shown in Fig. 12.
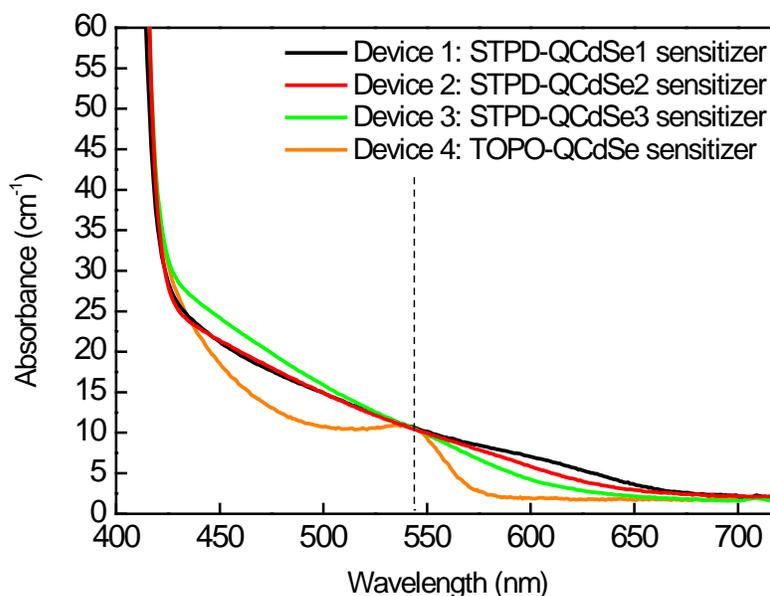
Fig. 12 Absorption spectra of active layers in PC devices.

For the photosensitization process to operate efficiently, the VB of the photosensitizer must occur lower in energy than that of the charge transporting matrix, TPD in this case. As such, upon absorption of a photon by QCdSe, an electron is promoted from its VB to its CB, resulting in an electron and a hole in the CB and VB, respectively.[21] Due to the relative position of their energy levels, it is energetically favorable for an electron in the VB of TPD to relax to the VB of QCdSe. As a result, the photogenerated electrons are associated with the CB of QCdSe and the holes are associated with the VB of TPD. Because the concentration of STPD-QCdSe is ~0.4 %, well below the percolation threshold, the holes associated with the TPD matrix will be the primary charge-transporting species.

The photoconductivity and dark conductivity for the PC devices are presented in Fig. 13 and 14. The devices photosensitized with STPD-QCdSe show significantly higher PC than does the device photosensitized with TOPO-QCdSe, while the dark conductivities of them are quite similar. No significant difference in the PC between devices 1, 2 and 3 can be observed. As a control, the PC and dark conductivities were also measured for TPD, void of any photosensitizer, under the same experimental conditions. Here, no detectable PC was observed while the dark conductivity was similar to that of other devices. In device 4, the photo-sensitizing TOPO-QCdSe is encapsulated by a layer of electrically insulative TOPO. This insulative layer acts as a barrier to the charge-transfer process between the QCdSe cores and the TPD matrix. In devices 1, 2 and 3, the QCdSe are encapsulated with STPD, and because STPD is conducive to the charge-transfer process, photo-excited charges are easily transferred from the QCdSe semiconductor core, through the ligands, and ultimately to the TPD charge-transporting
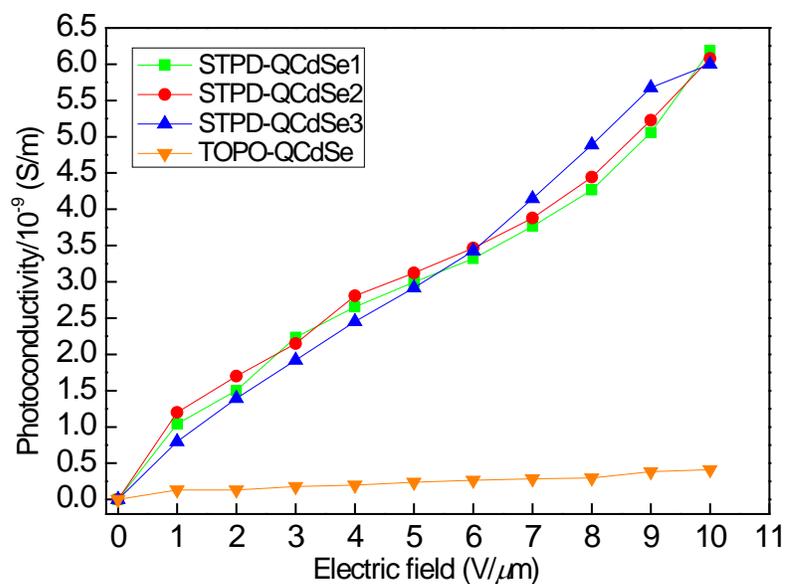
Fig. 13 Photoconductivities of composites.
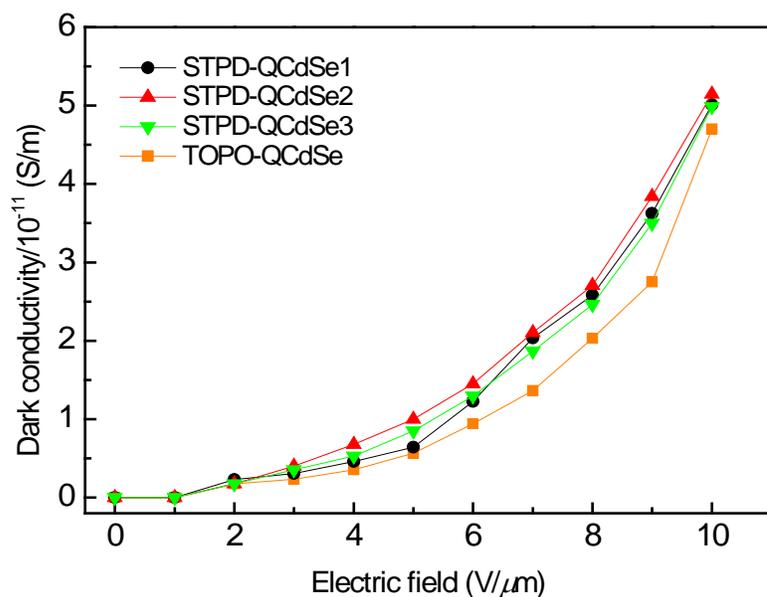
Fig. 14 Dark conductivities of composites.

matrix. As a result, the PC of these devices is greatly enhanced compared to that of device 4. The dark conductivity was not significantly influenced by the presence of the photo-sensitizers. Additionally, because the capping ligands have a molecular structure similar to that of the matrix, STPD-QCdSe is more easily dispersed in the matrix than is TOPO-QCdSe, which may also have a positive effect over the PC characteristics of the composite.

Conclusions

A relatively simple method for sulfonating TPD was developed and the sulfonated products can be used as passivating ligands in the synthesis of STPD-QCdSe. The sulfonated TPD is primarily mono-sulfonated. The UV-visible spectroscopy and PL spectroscopy results indicate that the sulfonation did not have a significant influence on TPD's electronic structure. The diameter of the synthesized STPD-QCdSe ranges from

3.1 to 3.9 nm and quantum confinement is observed in the UV-visible spectra. The newly developed STPD passivated QCdSe were used as a photo-sensitizer in STPD-QCdSe/TPD PC composites. A significant improvement in the PC of a STPD-QCdSe/TPD device was observed compared with that of a TOPO-QCdSe/TPD device (~ a factor of 15 at 10 V/μm) while dark conductivity of two types of composites were nearly identical.

Acknowledgments

Notes and References

1 D. V. Talapin, J. Lee, M. V. Kovalenko and E. V. Shevchenko, *Chem. Rev,* 2010, **110**. 389.

2 G. Konstantatos, I. Howard, A. Fischer, S. Hoogland, J. Clifford, E. Klem, L. Levina and E. H. Sargent, *Nature*, 2006, **442**. 180.

3 E. J. D. Klem, D. D. MacNeil, P. W. Cyr, L. Levina and E. H. Sargent, *Applied Physics Letter*, 2007, **90**. 183113.

4 V.L.Colin, M. C. Schlamp and A. P. Alivisatos, *Nature*, 1994, **370**, 354.

5 D. V. Talapin and C. B. Murray, *Science*, 2005, **310**. 86.

6 S. V. Voitekhovich, D. V. Talapin, C. Klinke, A. Kornowski and H. Weller, *Chem. Matter*, 2008, **20**. 4545.

7 N. C. Greenham, X. Peng and A. P. Alivisatos, *Physical Review. B*, 1996, **54**. 17628.

8 C. B. Murray, D. J. Noms and M. G. Bawendi, *J. Am. Chem. Soc,* 1993, **115**. 8706.

9 M. V. Jarosz, V. J. Porter, B. R. Fisherp, M. A. Kastner and M. G. Bawendi, *Physical Review B*, 2004, **70**, 195327.

10 V. J. Porter, S. Geyer, J. E. Halpert, M. A. Kastner and M. G. Bawendi, *J. Phys. Chem. C*, 2008, **112**. 2308.

11 Y. Shirota, *J. Mater. Chem*, 2000, **10**. 1-25.

12 M. Stolka, J. F. Yanus, D. M. Pai, *J. Phys. Chem*, 1984, **88**. 4707.

13 A. R. Kennedy, W. Ewen Smith, D. R. Tackley, W. I. F. David, K. Shankland, B. Brown and S. J. Teat, *J. Mater. Chem,* 2002. **12**. 168.

14 S. Wang, S. Yang, C. Yang, Z. Li, J. Wang and W. Ge, *J. Phys. Chem. B*, 2000, **104**. 11853.

15 C. Fuentes-Hernandez, J. Thomas, R. Termine, M. Eralp, M. Yamamoto, K. Cammack, K. Matsumoto, S. Barlow, G. Walker, G. Meredith, N. Peyghambarian, B. Kippelen and S. R. Marder, *Proceedings of SPIE-The International Society for Optical Engineering.* 2003, **5216**, 83.

16 S. Wang, Z. Zeng, S. Yang, L. Weng, P. C. L. Wong and K. Ho. *Macromolecules,* 2000, **33**. 3232.

17 L. Daniel, Klayman and T. S. Griffin, *J. Am. Chem. Soc*, 1973, **95**. 197.

18 S. H. Barbara, *Infrared Spectroscopy: Fundamentals and Applications*, John Wiley & Sons, Incorporated, 2004.

19 K. Surana, P. K Singh, H. Rhee and B. Bhattacharya, *J. Ind. Eng. Chem,* 2014, **1**. 19.

20 L. Liu, Q. Peng and Y. Li, *Inorganic Chemistry,* 2008, **47**. 5022.

21 S. Coe, W. Woo, M. Bawendi and V. Bulovic, *Nature*, 2002, **420**, 800.

22 Q. Xin, W. L. Li, G. B. Che, W. M. Su, X.Y. Sun, B. Chu and B. Li, *Appl. Phys. Lett*, 2006, **89 (22)**, 223524.

23 C. Li, X. Li, L. Cao, G. Jin and M. Gu, *Appl. Phys. Lett*, 2013, **102**, 251115.

24 J. R. I. Lee, R. W. Meulenburg, K. M. Hanif, H. Mattoussi and J. E. Klepeis, *PRL*, 2007, **98**, 146803

25 W. W. Yu, L. Qu, W. Guo and X. Peng, *Chem. Mater*, 2003, **15**. 2854.

26 R. W. Meulenberg, J. R.I. Lee, A. Wolcott, J. Z. Zhang, L. J. Terminello and T. V. Buuren, *A.C.S. NANO*, 2009, **3**. 325.

II. ENHANCEMENT IN THE PHOTOREFRACTIVE PERFORMANCE OF ORGANIC COMPOSITES PHOTOSENSITIZED WITH FUNCTIONALIZED CdSe QUANTUM DOTS

Yichen Liang, Wei Wang and Jeffrey G. Winiarz

Abstract

Enhancement in the photorefractive (PR) performance of organic composites photosensitized by CdSe quantum dots (QCdSe) passivated with the charge-transport ligands, sulfonated triphenyldiamine (STPD), is reported. This enhancement is primarily attributed to the ability of the passivating ligand, STPD, to facilitate the charge-transfer process between the QCdSe and the triphenyldiamine (TPD) charge-transport matrix. The PR composites exhibited a maximum photocharge-generation efficiency of 0.9% and two-beam coupling gain coefficient of 110 cm^{-1}. These figures of merit represent a significant improvement over similar composites photosensitized with more conventional trioctylphosphine oxide-passivated QCdSe (TQCdSe). Moreover, composites photosensitized with SQCdSe had a faster response time of $\tau = 128$ ms at an electric field of 60 V/μm compared with $\tau = 982$ ms for those containing TQCdSe. Because of the molecular similarity between the STPD passivating groups and the TPD-based charge-transport matrix, concentrations of up to 1.4 wt% of SQCdSe are achieved in PR composites without any detectable phase separation, a considerable improvement over the 0.7 wt% for TQCdSe.

1. Introduction

Increased attention has been paid to organic photorefractive (PR) composites which exhibit potential in numerous applications, e.g. updatable 3D displays, optical signal processing, and medical imaging [1]. Compared with more traditional PR materials, such as inorganic PR crystals, organic PR composites can be fabricated using relatively low-cost techniques, such as wet chemistry processes, and with significantly improved flexibility with regard to operational characteristics. Due to rapid advancements in organic syntheses, many types of organic semiconducting materials, e.g. polyvinyl carbozole (PVK), polyvinylindole and triaryl amine derivatives, have been developed and used as efficient charge-transport materials for PR composites [2,3]. The PR process is initiated when the photosensitizer absorbs a photon of appropriate energy resulting in the subsequent creation of free charge-carriers. Both organic and inorganic photosensitizers have been employed in conjunction with organic PR matrices. Of particular interest, semiconductor nanocrystals, also known as quantum dots (QDs), may be synthesized using facile methods such as colloidal synthesis and possess several unique properties including a tunable optical absorption and facilitation of charge-transport in organic composites [4]. To prevent aggregation, QDs are typically passivated by a layer of capping ligands during synthesis, e.g. trioctylphosphine oxide (TOPO), dodecanthiol, oleic acid, etc. In most cases these ligands are electrically inert and therefore act as an insulating barrier with respect to charge-transfer between the QD and the organic charge-transporting matrix, effectively decreasing the charge-generating efficiency of the QDs.

To address this impediment, techniques such as ligand exchange [5], chemical treatment [6], and heat annealing [7] have been explored. Although limited

enhancements in the charge-transfer process occurred, these methods are subject to drawbacks such as inefficient removal of the inert surfactants [8] or destabilization of the QDs [9]. Alternatively, derivatives of various charge-transporting species can be used as the passivating ligand directly in the synthesis of QDs. As an example, sulfonated PVK was used to passivate CdSe quantum dots (QCdSe) [10]. Compared to that passivated with 4-methylbenzebe thiol, QCdSe passivated with sulfonated PVK exhibited a significant improvement in the photosensitization of PVK-based PR composites, where a threefold increase in the two-beam coupling (TBC) gain coefficient, Γ, was observed [10]. Recently, sulfonated *N,N´*-Bis(3-methylphenyl)-*N,N´*-diphenylbenzidine (STPD), which is based on the charge transporting molecule *N,N'*-Bis(3-methylphenyl)-*N,N'*-diphenylbenzidine (TPD), and its successful use as the passivating ligand in the synthesis of QCdSe, has been described [11]. In that study, TPD composites photosensitized with STPD-passivated QCdSe (SQCdSe) showed a 15-fold increase in photoconductivity, σ_p, over TPD composites photosensitized with more conventional QCdSe passivated with trioctylphosphine oxide or TOPO (TQCdSe). Motivated by these promising data, this study investigates the ability of SQCdSe to photosensitize PR composites based in TPD, and the fundamental processes associated with the formation of a PR grating. As such, the PR composites were designed using TPD as the primary charge-transport material, and 2-[4-bis(2-methoxyethyl) amino] benzylidenemalononitrile (AODCST) as the nonlinear optical (NLO) chromophore. A small amount of PVK was included to prevent phase separation of the TPD and AODCST. Because the STPD capping ligands are chemically similar to the charge-transporting matrix, composed largely of TPD, the SQCdSe are highly soluble in the PR composite, and a relatively high concentration of

1.4 wt% was achieved without any detectable aggregation. In contrast, aggregation of TQCdSe was detected for concentrations exceeding ~0.7 wt%. A substantial enhancement in the PR performance was achieved for devices photosensitized with SQCdSe relative to those utilizing TQCdSe or C_{60}.

2. Experimental Methods

2.1. Materials

TPD was purchased from Magical Scientific Corporation. Cadmium acetate dihydrate (98%), cadmium oxide (99.5%), selenium powder (100 mesh, 99.99%), sodium borohydride (98%), acetic anhydrate (99+%), fullerene-C_{60} (99.9%), trioctylphosphine oxide (99%), trioctylphosphine (90%), methanol (99%), ethanol (99%), 1-pentanol (99%), acetone (99%) and 1.2-dichlorobenzene (99%) were purchased from Sigma Aldrich Corporation. Sulfuric acid (95%-98%) was purchased from Alfa Aesar Corporation. All chemicals were used as received without further purification. Glass beads with a 50 μm diameter were purchased from MO-Sci Corporation. Glass slides with 120 nm indium tin oxide (ITO) coating were purchased from Colorado Concept Coating LLC.

2.2. Synthesis of SQCdSe

STPD (115 mg) was synthesized according to literature [11] and dissolved in a mixture of 1-pentanol (1.5 ml) and 1,2-dichlorobenzene (1.5 ml). This solution was then combined with cadmium acetate dissolved in ethanol (150 μl, 0.15 M) and heated to 120 °C. Subsequently, NaHSe stock solution (200 μl, 0.12 M), prepared using techniques

found in literature [11], was swiftly injected into the Cd^{2+}/STPD solution, forming orange-red aggregates at the bottom of the reactor presumed to be SQCdSe. The SQCdSe was separated from the solvent and could be homogenously suspended in acetone. To purify the SQCdSe, the SQCdSe/acetone suspension was centrifuged at 15000 rpm, the supernatant was decanted and discarded, and the remaining residue was re-suspended in distilled acetone. This procedure was repeated several times to remove any unreacted starting material. To remove larger particles and aggregates, the purified SQCdSe/acetone was centrifuged at 900 rpm, the supernatant was collected for future use and any residue was discarded. TQCdSe and AODCST were synthesized using methods reported in literature [12,13].

2.3. Fabrication of PR Devices

The required constituents, including TPD, PVK, AODCST were dissolved in toluene, and filtered using Whatman qualitative filter paper (Grade 5), followed by the addition of the desired photosensitizer. After thorough mixing via vortex, the solvent was evaporated under vacuum and the solid residue was collected. This residue was heated beyond its melting temperature (235 - 250 °C), sandwiched between two pieces of ITO coated glass slides and cooled to room temperature. The thickness, d, of the PR films was maintained at 50 μm using glass beads. Six PR devices were fabricated and their compositions are detailed in Table 1. Devices photosensitized with SQCdSe, TQCdSe, and C_{60} are labeled as DS, DT, and DC, respectively. Numerical labels following the notations indicate the weight percentage of the photosensitizers, e.g., DS07 indicates the device was sensitized by 0.7 wt% SQCdSe. D0 contained no photosensitizer and served as a control.

Table 1. The compositions of the PR films used in this study.

Devices	TPD wt%	PVK wt%	AODCST wt%	SQCdSe wt%	TQCdSe wt%	C60 wt%
DS07	59.3	10.0	30.0	0.7	0	0
DS10	59.0	10.0	30.0	1.0	0	0
DS14	58.6	10.0	30.0	1.4	0	0
DT07	59.3	10.0	30.0	0	0.7	0
DC05	59.5	10.0	30.0	0	0	0.5
D0	60.0	10.0	30.0	0	0	0

2.4. Materials Characterizations

The absorption spectra of the photosensitizers and PR devices were acquired with a Cary 50 UV/visible spectrophotometer. The photosensitizers were dissolved in toluene with a concentration of 0.1 mg/ml. For SQCdSe, it was necessary to include 20 vol% acetone to form a stable suspension.

Thermal gravimetric analysis (TGA), performed on a TA Instruments Q50 Thermogravimetric Analyzer in an N_2 environment, was used to quantify the degree to which the CdSe nanocrystalline cores were passivated with organic STPD or TOPO ligands. TGA samples were dried for 24 h under vacuum at room temperature prior to analysis.

The microstructures of the PR composites were characterized using a Helios Nano Lab 600 scanning electron microscope. Cross sections of the PR films were imaged with an accelerating voltage of 10 kV and beam current of 43 pA. The working distance was set at 4.5 mm and secondary electron mode was employed. The electron beam was incident on the sample with a tilt angle of 20º.

All conductivity, σ, and PR characterizations were conducted using a He-Ne laser operating at $\lambda = 543$ nm. The σ were measured with a Keithley electrometer using a dc-photocurrent technique and were calculated according to the equation

$$\sigma = J/E, \tag{1}$$

where J is the current density and E is the externally applied electric field. For calculations of σ_p, the dark current density was subtracted from the photo-current density. For σ_p characterizations, the beam had a power of 0.4 mW and a diameter of 1.5 mm. The photo-charge generation quantum efficiencies, Φ, were determined using the equation

$$\Phi = \frac{N_{cc}}{N_{ph}} = \frac{\sigma_p hcE}{Ie\lambda\alpha_{543}d}, \tag{2}$$

where N_{cc} and N_{ph} are the numbers of photo-generated mobile charge-carriers and absorbed photons, respectively, h is Planck's constant, c is the speed of light, I is the intensity of the incident beam, e is the elementary charge, and α_{543} is the optical absorbance of the PR device at 543 nm [14].

For TBC experiments, the writing beams were p-polarized with intensities of $I_1 = 0.2$ and $I_2 = 1.2$ mW/cm^2 and incident angles of $\theta_1 = 40°$ and $\theta_{ref} = 70°$ relative to the sample normal. This geometry was used in an effort to optimize the TBC gain coefficient, Γ, which was calculated using the equation

$$\Gamma = [\ln(\gamma\beta) - \ln(\beta + 1 - \gamma)]/L, \tag{3}$$

where γ is the ratio of the intensities of the beam experiencing gain with and without the pump beam, β is the intensity ratio of the two writing beams, and L is the path length in the PR medium where TBC occurs [1].
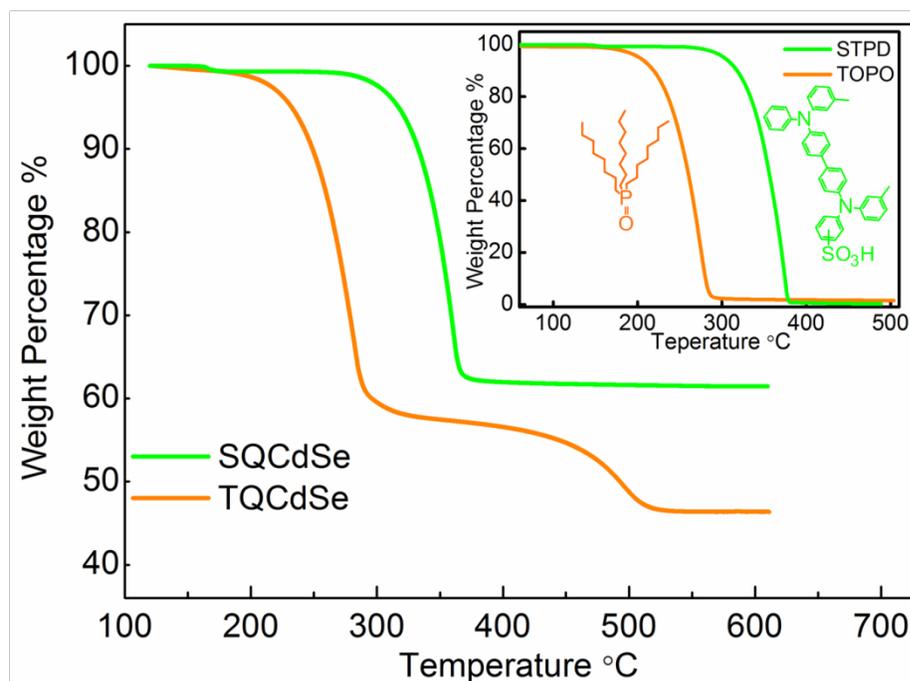
3. Results and Discussion

Fig. 1. TGA of TQCdSe and SQCdSe. The inset shows the TGA of STPD and TOPO.

The TGA of SQCdSe and TQCdSe as well as that of the capping ligands, STPD and TOPO, are shown in Fig. 1. Evident in the inset, STPD and TOPO experience mass losses at 190 °C and 290 °C, respectively. Because the TGA were conducted in an N_2 environment, these mass losses are attributed to the thermal evaporation of STPD and TOPO. The TGA trace for TQCdSe shows two distinct regions of mass loss. The first loss occurs at 195 °C with 44% reduction in mass. This loss occurs close to the thermal evaporation temperature of TOPO and is therefore attributed to the vaporization of the TOPO surfactant. Another 8% reduction in mass occurs at 435 °C, which is likely attributable to the thermal evaporation of TOPO more firmly attached to the surface of QCdSe through covalent bonding. Similar behavior has been observed in PbS QDs passivated with oleic acid [14]. With regard to SQCdSe, a 38% reduction in mass occurs

at 290 °C, coinciding with the thermal evaporation temperature of STPD, and no further loss in mass is observed. These data suggest that the strong bonding that exists between a small fraction of the TOPO and the QCdSe cores is absent in the case of SQCdSe. Based on the TGA results, the weight percentages of inorganic CdSe in SQCdSe and TQCdSe are 61% and 45%, respectively. Because SQCdSe and TQCdSe were synthesized such the spectroscopic peak associated with their first exciton is located at $\lambda \approx 543$ nm, it is assumed that their average diameters are identical and calculated as 3.2 nm based on the empirical equation

$$D = (1.6122 \times 10^{-9})\lambda^4 - (2.6575 \times 10^{-6})\lambda^3 + (1.6242 \times 10^{-3})\lambda^2 - (0.4277)\lambda + 41.57, \tag{4}$$

where D is the diameter of QCdSe [15]. Assuming that the inorganic CdSe core in both SQCdSe and TQCdSe has a density identical to that of the bulk (5.82 g/cm^3), [16,17] the average number of capping ligands per nanoparticle in SQCdSe and TQCdSe can be estimated as 62 and 151, respectively, for a surface density of 1.9 and 4.7 ligands/nm^2, respectively, which is similar to values reported in literature [18]. The significant difference in surface density is likely attributable to the large steric volume associated with the abundance of bulky phenyl groups in STPD (see Fig. 1).

Owing to the chemical similarity between STPD and TPD, SQCdSe was more soluble in the TPD-based PR composites than TQCdSe, as revealed by the SEM images in Fig. 2. Evident in Fig. 2 (A), which depicts the cross section of the DS14 PR film, a loading content of 1.4 wt% SQCdSe could be achieved in the PR composite without any detectable phase separation. Similarly, Fig. 2 (B) depicts the cross-section of DT07

illustrating the lack of phase separation for TQCdSe at a loading content of 0.7 wt%. For concentration of TQCdSe greater than 0.7%, however, phase separation is apparent as shown in Fig 2 (C) (TPD:PVK:AODCST:TQCdSe = 59.1:10.0:30.0:0.9 wt%). Evident in the figure, micro-sized aggregates (some marked by red circles) segregated from the matrix. Confirmed by the energy-dispersive X-ray spectroscopy (EDS) shown in Fig. 3, the aggregate phase was found to be composed of CdSe. For the purposes of comparison, the cross-section of D0 is shown in Fig. 2 (D) where micro-level phase separation is not observed.
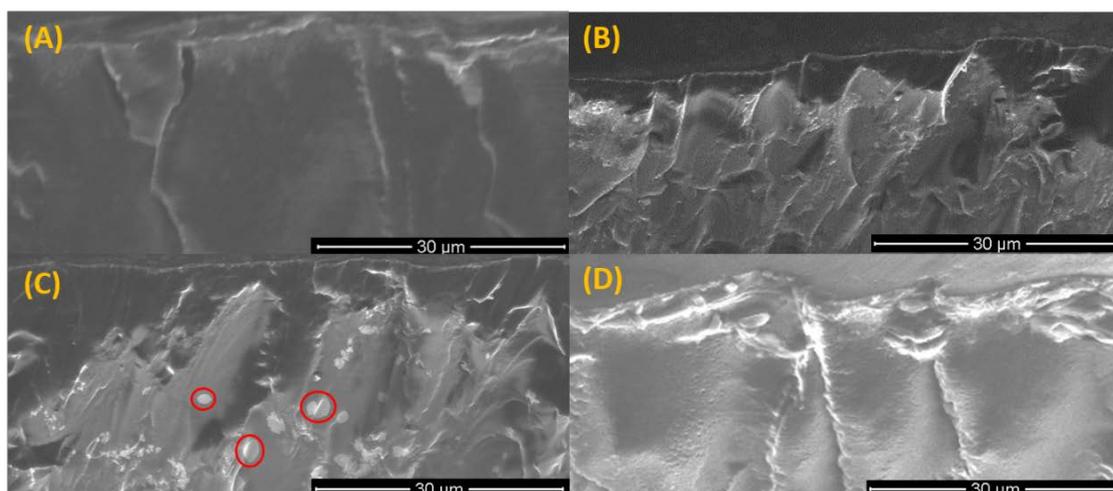

Fig. 2. SEM cross section images of PR composites. (A) cross-section of DS14, (B) cross-section of DT07, (C) cross-section of a PR film with composition of TPD:PVK:AODCST:TQCdSe = 59.1:10.0:30.0:0.9 wt% TQCdSe, (D) cross-section of D0.
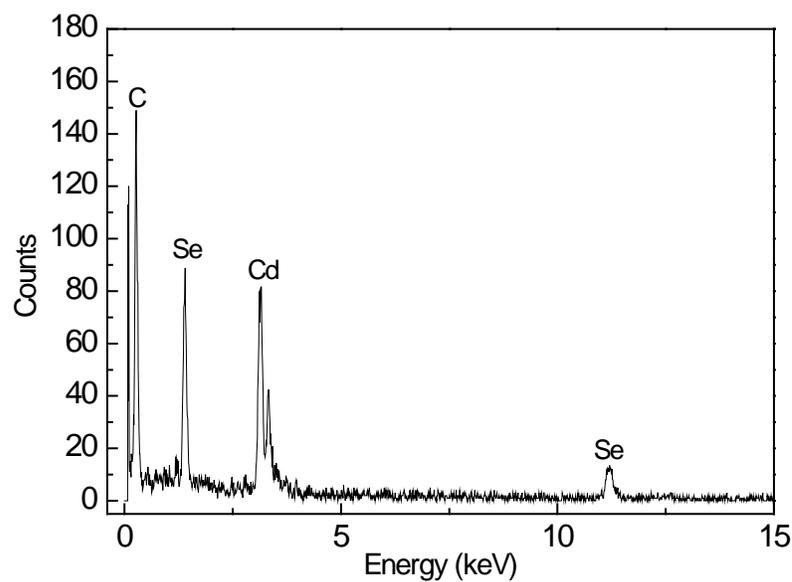
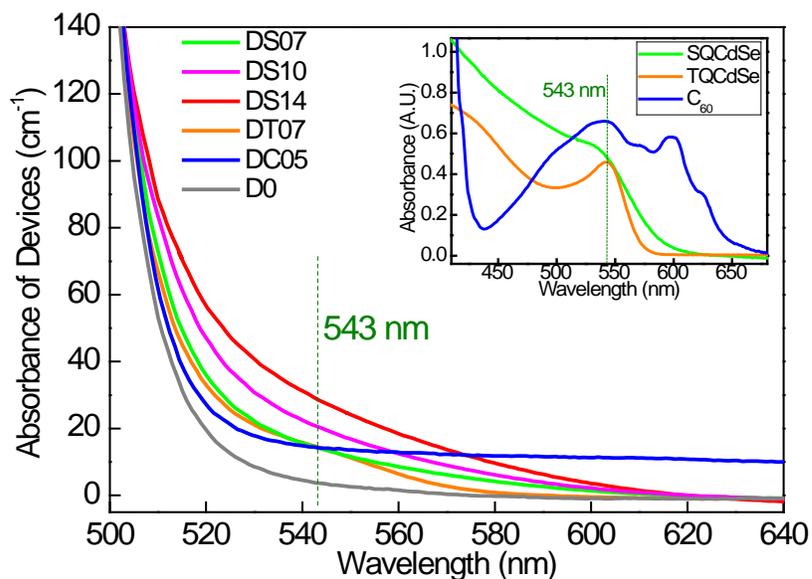Fig. 3. EDS of the CdSe aggregates shown in Fig. 2 (C).

Fig. 4. Visible absorption spectra of the PR devices. The inset depicts the normalized visible absorption spectra of the photosensitizers utilized in this study.

The visible absorption spectra of SQCdSe, TQCdSe and C_{60} are shown in the inset of Fig 4. The size of SQCdSe and TQCdSe was fashioned so that the absorption

peak/shoulder would occur at ~543 nm, the same wavelength at which the PR characterizations were conducted. At identical concentrations by mass (including both inorganic QCdSe and the organic capping group), SQCdSe and TQCdSe showed nearly equal absorbance at 543 nm. However, as revealed by TGA, the proportion of the inorganic CdSe in SQCdSe was 29.2% higher than that of TQCdSe, and therefore SQCdSe contained a larger portion of the light-absorbing QCdSe. At the same time, as reflected in the inset of Fig. 1, TQCdSe exhibited a higher degree of monodispersity than did SQCdSe, and so even though there was more QCdSe in the SQCdSe, the TQCdSe absorbed more efficiently at 543 nm. These countervailing effects between the greater concentration and the greater absorbing efficiency led to nearly equal absorbance per unit mass of suspended SQCdSe and TQCdSe at 543 nm.

The visible absorption spectra of PR devices are depicted in Fig. 4. D0, which does not contains an added photosensitizer, has an absorbance at 543 nm of $\alpha_{543} = 2.7$ cm^{-1}, attributed primarily to AODCST (see supplemental for absorption spectrum of AODCST). For devices photosensitized with SQCdSe, DS07, DS10 and DS14, $\alpha_{543} = 15$ cm^{-1}, 21 cm^{-1}, and 29 cm^{-1}, respectively. To make a direct comparison of the performance of each photosensitizer, devices containing TQCdSe or C60 which had a similar α_{543} as DS07 were fabricated and labeled as DT07 and DC05.

Fig 5 illustrates the σ_p as a function of E for each PR device, with the inset showing their dark conductivities, σ_d. A critical step in the PR process involves the reorientation of the chromophores in the PR matrix, which is initiated by the establishment of an internal space-charge field, E_{sc}, which is related to σ_p/σ_d, as

$$|E_{sc}| = mE_q \left[\frac{E_0^2 + E_d^2}{E_d^2 + (E_d + E_q)^2}\right]^{1/2} \frac{1}{1 + \frac{\sigma_d}{\sigma_p}}, \tag{5}$$

where m is the depth of modulation, E_0 is the component of E coincident with the grating vector, E_q is the trap-density-limited spatial charge field, and E_d is the diffusion field [19,20]. Evident from Fig. 5 and Fig. 6 is that DS10 shows the highest σ_p as well as the highest σ_p/σ_d. As seen in the data for DS07, a small reduction in the concentration of SQCdSe resulted in a corresponding reduction in σ_p, which is due to the decrease in the number of photo-generated charges. The σ_d however was largely unaffected by the decrease in the concentration of SQCdSe and therefore a decrease in σ_p/σ_d also resulted. An increase in the concentration of SQCdSe relative to DS10, as in DS14, however, resulted in an increase in the σ_d, especially at $E > 40$ V/μm. This effect may be attributed to the fact that the photosensitizer has a higher charge-carrier mobility, μ ($\mu_{TPD} \approx 6 \times 10^{-5}$ cm^2/(Vs) [21] and $\mu_{CdSe} \approx 0.01$ cm^2/(Vs) [22]), and can effectively participate the charge-transport process. Previous research has demonstrated that this effect becomes pronounced when the QD concentration reaches a certain threshold due to the formation of electronic double layers at the boundary between QD clusters and charge-transporting matrix [23], and is more significant at relatively large E [24,25]. Typically in PR composites, this threshold is around 1.0 wt% [24-26]. This increase in σ_d was not accompanied by a significant increase in σ_p for DS14, consequently, σ_p/σ_d was drastically decreased, especially at $E > 40$ V/μm. These data indicate ~1.0 wt% is a nearly optimized concentration of SQCdSe for this composition in PR applications. It is noteworthy that all DS devices photosensitized with SQCdSe display superior σ_p and σ_p/σ_d relative to those utilizing TQCdSe, demonstrating the ability of STPD to enhance the efficiency of charge-transfer between the inorganic QCdSe and the photoconductive

organic matrix. Devices photosensitized with SQCdSe also exhibited photoconductive performance superior to that photosensitized with C_{60}, particularly at low E. These data suggest the potential for this novel class of photosensitizers to replace more traditional photosensitizers in PR or photoconductive composites, particularly for applications requiring relatively low E.
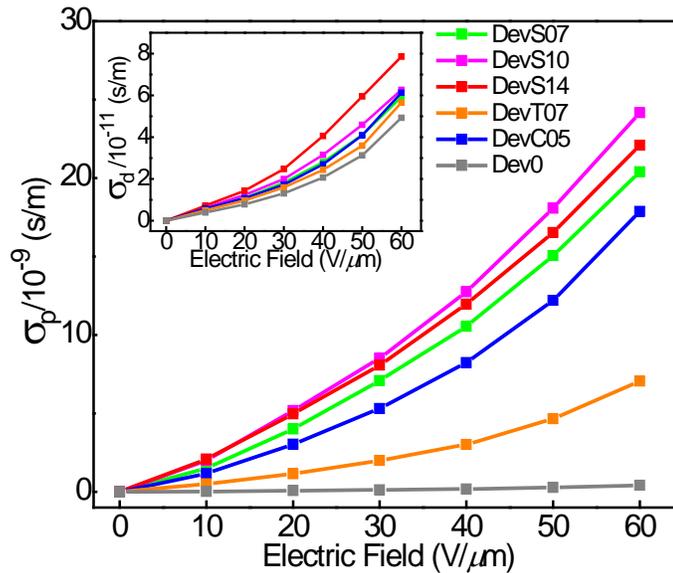

Fig. 5. Photoconductivity, σ_p, as a function of the electric field, E. The inset shows the dark conductivity, σ_d as a function of the electric field, E.

The Φ were determined according to eq. 2 and are presented as a function of E in Fig. 7. Evident from the figure, DS07 and DS10 exhibit similar trends in Φ across the range of E, indicating that Φ is independent of concentration. The Φ of DS14, however, is diminished relative to that of DS07 and DS10, which may be attributed to an increase in the concentration of deep charge-traps in the composite accompanying the increase in concentration of SQCdSe [27-30]. The deep charge-traps may originate from surface defects associated with QCdSe [28,29], which may be present due to the relatively
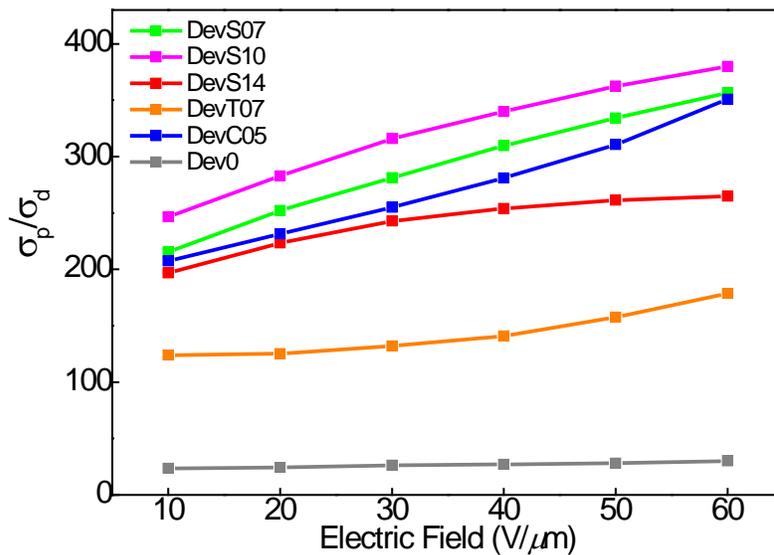
Fig. 6. Ratio of photoconductivity to dark conductivity, σ_p/σ_d, as a function of electric field, E.
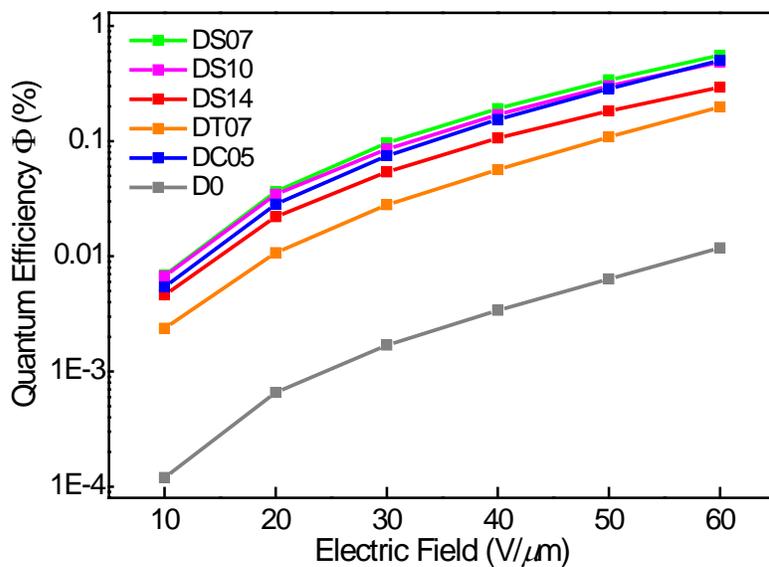

Fig. 7. Quantum efficiency, Φ, as a function of electric field, E.

inefficient passivation of SQCdSe as indicated by the TGA. All the SQCdSe photosensitized devices exhibit Φ significantly greater than that of DT07 across the

range of *E*. This indicates that the improved performance associated with SQCdSe photosensitized devices is primarily rooted in an enhanced generation of free charge-carriers. This enhanced charge-carrier generation can be traced to the elimination of the insulative barrier associated with traditional inorganic photosensitizers such as TQCdSe, and the subsequently increased number of holes which ultimately can become associated with the charge-transport matrix.
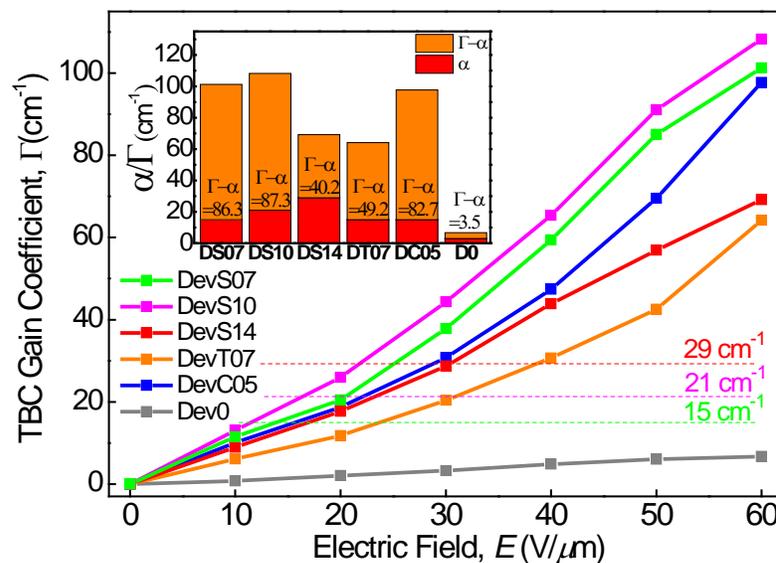

Fig. 8. TBC gain coefficient, Γ, as a function of electric field, *E*. The inset shows the Γ-α at *E* = 60 V/μm.

A unique feature of the PR effect is that the diffraction grating is spatially shifted from the light intensity pattern by $\pi/2$, which results in an asymmetrical transfer of energy between the writing beams [1], distinguishing the non-local PR grating from other local gratings, e.g. photo-bleaching. The PR nature of the diffraction gratings generated in the studied devices was confirmed using conventional TBC and the Γ are

illustrated as a function of E in Fig. 8. Comparing these results with those presented in Fig. 5 & 6 reveals a clear correlation between the photoconductive and PR performances. Specifically DS10, which exhibited the highest σ_p/σ_d, also showed the largest values of Γ. A slight decrease in Γ is observed for DS07 relative to that of DS10 while the decrease is more significant for DS14. This too, corresponds with the trends observed for the σ_p/σ_d. The significant decrease in Γ and in σ_p/σ_d observed for DS14 may be attributable to an increase in the density of deep charge-traps. As with the σ_p/σ_d, all of the SQCdSe photosensitized devices exhibited a higher Γ than DT07 across the entire range of E owing to the charge-transfer capability of STPD. It is also noted that at the same absorbance of 15 cm^{-1}, the TBC performance of the DS07 exceeds that of DC05, further affirming the ability of SQCdSe to rival the traditional photosensitizer C$_{60}$ at 543 nm in PR applications. For the control device, D0, a maximum $\Gamma = 6.7$ cm^{-1} was measured at $E = 60$ V/μm, which is ~6% of the Γ in DS10, and ~10% of that in DT07 at the same E. This implies the small absorbance in D0 from AODCST is sufficient to induce a PR response. However, compared with the devices containing extrinsic photosensitizers, the TBC in D0 is relatively insignificant. For practical applications, it is desirable to have $\Gamma > \alpha$. As shown in the inset of Fig. 6, the net gain coefficient, Γ-α, is positive in DS07, DS10, and DC05 for $E \geq 20$ V/μm. Similarly, DT07 and DS14 exhibit a positive Γ-α for $E \geq 30$ V/μm. At $E = 60$ V/μm, DS10 shows the highest Γ-$\alpha = 87.3$ cm^{-1}.
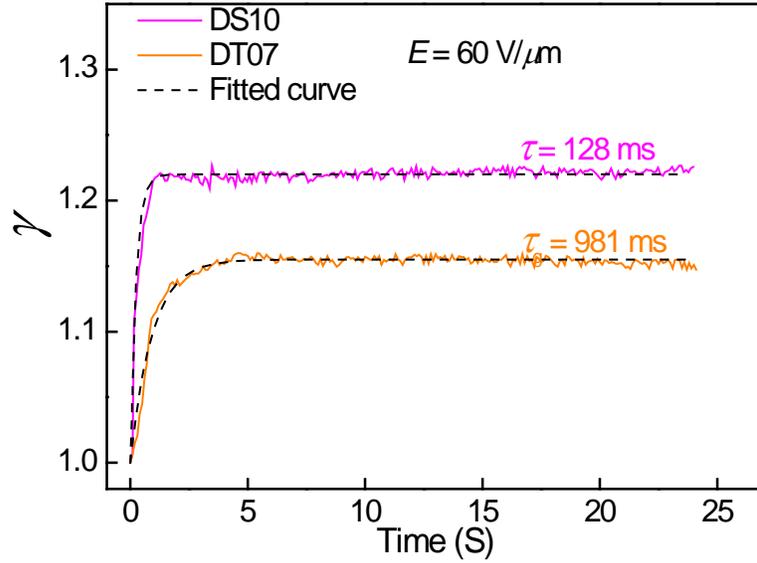
Fig. 9. Optical gain factor, γ, as a function of time, t, at $E = 60$ V/μm.

To compare the dynamic response of the PR devices sensitized by SQCdSe and TQCdSe, the optical gain factors, γ (see eq. 3), of DS10 and DS07 were measured as a function of time with $E = 60$ V/μm, and the results are shown in Fig. 9. The evolution of the PR grating follows the equation

$$\gamma(t) = 1 + (\gamma_0 - 1)\{1 - \exp[-(t - t_0)/\tau]\} \tag{6}$$

where γ_0 is the steady state γ, τ is the characteristic response time, and t_0 is time when the writing of the PR grating is initiated. [31] As evident in the figure, DS10 exhibited a faster τ, as well as a higher value of γ relative to DT07. By fitting the data to eq. 6, the response times of DS10 and DS07 were determined as $\tau = 128$ and $\tau = 981$ ms, respectively. The significant decrease in PR growth time for DS10 is largely attributed to an enhancement in the charge-transfer process between the SQCdSe photosensitizer and the TPD charge-transporting matrix as facilitated by the STPD charge-transfer ligands.

4. Conclusion

In summary, the performance of TPD-based PR composites was significantly improved through the utilization of SQCdSe as the photosensitizer. As a result of the superior solubility of SQCdSe in the TPD-based matrix as well as the enhanced charge-transfer efficiency between the photosensitizer SQCdSe and the charge-transport matrix, the PR composites photosensitized with SQCdSe exhibited superior photo-charge generation efficiencies, TBC gain coefficients, and PR response times relative to similar composites photosensitized with TQCdSe. It was further demonstrated that SQCdSe can compete with more traditional photosensitizers, such as C60, in high performance PR composites, particularly at relatively low E. To fully exploit this approach, the ability of STPD to passivate other types of QDs, and further the performance of other STPD-passivated QDs in photosensitizing PR materials is under current investigation.

References

1) S. Köber, M. Salvador, K. Meerholz, Adv. Mater. 23 (2011) 4725.

2) E. Mecher, F. Gallego-Gomez, H. Tillmann, H. Horhold, J. Hummelen, K. Meerholz, Nature 418 (2002) 959.

3) K. Ogino, T. Nomura, T. Shichi, S. Park, H. Sato, T. Aoyama, T. Wada, Chem. Mater. 9 (1997), 2768.

4) K. Choudhury, J. Winiarz, M. Samoc, P. Prasad, Appl. Phys. Lett. 82 (2003) 406.

5) J. Winiarz, J. Phys. Chem. C 111 (2007) 1904.

6) M. Jarosz, V. Porter, B. Fisherp, M. Kastner, M. Bawendi, Phys. Rev. B 70 (2004) 195327.

7) V. Porter, S. Geyer, J. Halpert, M. Kastner, M. Bawendi, J. Phys. Chem. C 112 (2008) 2308.

8) C. Murray, D. Noms, M. Bawendi, J. Am. Chem. Soc. 115 (1993) 8706.

9) D. Talapin, C. Murray, Science 310 (2005) 86.

10) J. Park, O. Park, Apply. Phys. Lett. 89 (2006) 193101.

11) Y. Liang, J. Moon, R. Mu, J. Winiarz, J. Mater. Chem. C, 3 (2015) 4134.

12) C. Murray, D. Norris, M. Bawendi, J. Am. Chem. Soc. 115 (1993) 8706.

13) D. Wright, M. Díaz-García, J. Casperson, M. DeClue, W. Moerner, R. Twieg, Appl. Phys. Lett. 73 (1998) 1490.

14) J. Moon, Y. Liang, T. Stevens, T. Monson, D. Huber, B. Mahala, J. Winiarz, J. Phys. Chem. C 119 (2015) 13827.

15) W. Yu, L. Qu, W. Guo, X. Peng, Chem. Mater. 15 (2003) 2854.

16) M. Marcus, W. Flood, M. Stiegerwald, L. Brus, M. Bawendi, J. Phys. Chem. 95 (1991) 1572.

17) S. Rosenthal, J. McBride, S. Pennycook, L. Feldman, Surf. Sci. Rep. 62 (2007) 111.

18) V. Amin, K. Aruda, B. Lau, A. Rasmussen, K. Edme, E. Weiss, J. Phys. Chem. C 119 (2015) 19423.

19) N. Kukhtarev, V. Markov, S. Odulov, M. Soskin, V. Vinetskii, Ferroelectrics 22 (1979) 949.

20) W. Moerner, S. Silence, F. Hache, G. Bjorklund, J. Opt. Soc. Am. B 11 (1994) 320.

21) K. Ogino, T. Nomura, T. Shichi, S. Park, H. Sato, Chem. Mater. 9 (1997) 2768.

22) E. Talgorn, R. Abellon, P. Kooyman, J. Piris, T. Savenije, A. Goossens, A. Houtepen, L. Siebbeles, ACS Nano 4 (2010) 1723.

23) T. Zhuravleva, O. Ivanova, E. Krinichnaya, I. Misurkin, S. Titov, S. Zav'yalov, E. Grigor'ev, Russ. J. Phys. Chem. B 5 (2011) 681.

24) J. Winiarz, L. Zhang, M. Lal, C. Friend, P. Prasad, Chem. Phys. 245 (1999) 417.

25) D. Steenwinckel, E. Hendrickx, A. Persoons, J. Chem. Phys. 114 (2001) 9557.

26) O. Ostroverkhova, W. Moerner, Chem. Rev. 104 (2004) 3267.

27) F. Aslam, D. Graham, D. Binks, P. Dawson, N. Pickett, P. O'Brien, C. Byeon, D. Ko, J. Lee, J. Appl. Phys. 103 (2008) 093702.

28) D. Binks, S. Bant, D. West, P. O'Brien, M. Malik, J. Modern Opt. 50 (2003) 299.

29) F. Aslam, D. Rahn, D. West, P. O'Brien, N. Pickett, S. Daniels, J. Chem. Phys. 122 (2005) 184713.

30) T. Fears, C. Anderson, J. Winiarz, J. Chem. Phys. 129 (2008) 154704.

31) A. Vannikov, A. Grishina, High Energ. Chem. 41 (2007) 162.

Appendix
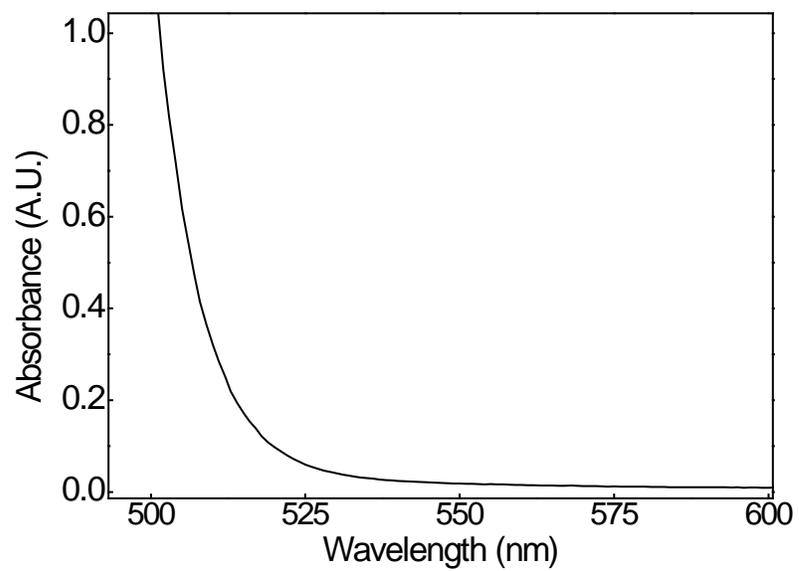
Supplement Fig. 1. Absorption spectrum of saturated AODCST solution in toluene.

III. PRACTICAL CORRECTION OF A PHASE-ABERRATED LASER BEAM USING A TPD-BASED PHOTOREFRACTIVE COMPOSITE

Yichen Liang and Jeffrey G. Winiarz

Abstract: A photorefractive composite based on a triphenyl-diamine derivative was used to restore a severely phase-aberrated laser beam to a nearly aberration-free state. Here, a forward degenerate four-wave mixing (DFWM) geometry was employed for the elimination of phase-distortions and its practical applicability in the transmission of optically encoded data is demonstrated. Conventional two-beam coupling (TBC) and DFWM experiments were used to characterize the composite subject to the current experimental setup. The TBC net gain coefficient was 100 cm^{-1} with an applied external electric field of 70 V/μm. Internal and external diffraction efficiencies of 10% and 6%, respectively, were observed with a similar external electric field. Using time-resolved DFWM, the growth rate of the photorefractive grating was recorded as 0.51 s.

Research in optical communications progressed swiftly in the late 20th century due to rapid advancements in laser technology. Unfortunately, aberrations arising from imperfections in the transmission media (e.g. atmosphere, optical fiber, etc.) pose a critical issue because they lead to degradation of the transmitted signal. Several techniques involving adaptive optics have been developed to address this issue [1, 2]. These techniques, however, are costly and require complicated electronics. In contrast, holographic techniques using photorefractive (PR) elements offer a simple approach and are relatively cost-effective [3-5]. Previous research has demonstrated that, due to the

absence of phase cross talk between the two writing beams, inorganic PR crystals can be used for the elimination of phase aberrations using two-wave mixing processes [6, 7]. In contrast, organic PR composites provide an attractive alternative to inorganic crystals due to their low cost, ease of processability, and tunability of electrical and optical properties through modification of chemical composition [8, 9].

Preliminary proof-of-concept experiments involving organic PR composites have shown great potential for use in the elimination of phase aberrations. Specifically, an organic PR composite, acting as a phase-conjugate mirror, has been used in the elimination of phase aberrations in an optical beam [3]. However, the geometry used in this demonstration precludes it from being used to transmit a signal from a sender to a receiver at a remote location. Here, an optical signal originating at the sender was passed through an aberrating medium and subsequently the phase conjugate signal was redirected back to the sender through the original aberraing medium. More recently an optical system based on a forward degenerate four-wave mixing (DFWM) geometry in which the signal was sent from a sender to a remotely located receiver has been described [4]. It was also demonstrated that such an optical system can be used in the correction of dynamic phase aberrations [5]. Nevertheless, the geometry used in those demonstrations lacks practical applicability in that a coherent, unaberrated reference beam was required to be transmitted from the sender to the receiver. In real applications, such a requirement is impractical because the object and reference beams (OB and RB, respectively) would be subjected to the same aberrating transmission medium. Thus, any aberration arising in the OB would also be present in the RB.

To overcome these shortcomings, a novel optical system detailed schematically in Fig 1 is introduced. As seen in the figure, previously unrealized practical applicability is achieved in that this configuration is comprised of a distinct sender and receiver, separated by an aberrating medium traversed by a single optical beam. In this model, an optical signal is encoded in a laser beam by the sender. This information is subsequently transmitted through an aberrating medium, represented in the figure by AB, which has the effect of degrading the phase quality of the encoded information. Here, the aberrating medium was fabricated by spreading epoxy across a microscope slide. Finally, the aberrated information-carrying beam reaches the receiver where the information can be reconstructed, free of aberrations, using the optical system described herein in conjunction with a suitable PR device.

A He-Ne laser operating at a wavelength of 633 nm with s-polarization (500:1) was used for all experiments. A polarizing beam splitter (PBS) further filtered any p-polarization. The beam diameter at the object, an Air Force resolution target (AF) in this case, was adjusted with Lens 1 (L1). Here, the 0.5 mm sized figures from the AF were imaged (see Fig. 2). L2, L3 and L6 were used to adjust the size of the beam at the respective optical components. The signal beam was divided into OB and RB using a 50:50 beam splitter (BS). The polarization of OB could be continuously rotated by an angle, ϕ, away from s-polarization ($\phi = 0°$ is maximized s-polarization, $\phi = 90°$ is maximized p-polarization) via a half-wave plate (HP). A neutral-density filter (ND) was used to adjust the intensity of OB. To produce a
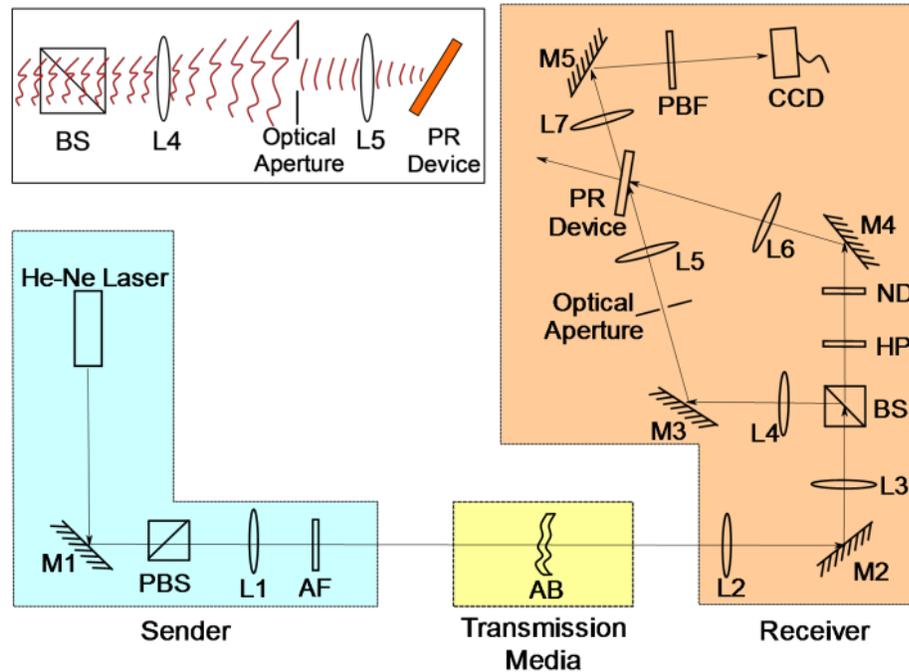
Fig. 1. Schematic diagram depicting the optical system. M denotes mirror. The numbers in the parentheses indicate the distance (cm) of each component from the PR device as measured along the relevant beam path. Laser (-224); M1 (-179); PBS (-161); L1 (-76), f=25 cm; AF (-68); AB (-67); L2 (-62), f=7.5 cm; M2 (-58); L3 (-52) f=7.5 cm; BS (-46.5); L4 (-37), f=5 cm; HP (-43); ND (-40.5); M3 (-32); M4 (-32.5); Optical aperture (-21); L5 (-15), f=15 cm; L6 (-16), f=10 cm; L7 (15.5), f=10 cm; M5 (27); PBF (40); CCD (45). The inset illustrates the mechanism of reducing the aberrations associated with RB.
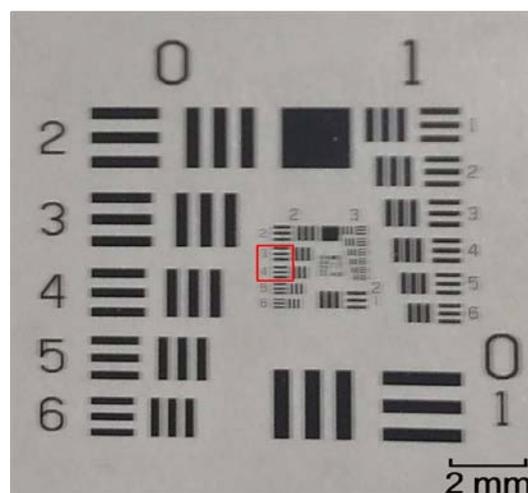

Fig. 2. Air Force resolution target used as the imaged object, the imaged part is marked by the red rectangular

RB which was relatively free of aberrations, RB was first expanded using L4 to a diameter of ~3 mm and subsequently passed through an optical aperture with a diameter of ~1 mm, allowing for a relatively "clean" portion of RB to be isolated. A schematic of this process is shown in the inset of Fig. 1. The diameter of RB at the PR device was finally adjusted using L5. For all experiments herein, OB and RB had beam areas of 0.12 cm^2 and intensities of 14.72 and 7.31 mW/cm^2, respectively, at the PR device, unless otherwise noted. The writing beams, OB and RB, intersected at an angle of 35° in air at the PR device. The angle between the PR device normal and the beam bisector was 40°. These angles were experimentally determined to optimize the quality of the restored image. A polarizing beam filter (PBF) was placed after the PR device at the position indicated in Fig. 1, allowing only the *p*-polarized portion of OB, diffracted by the PR grating, to pass and polarized portion of OB is referred to as the information beam (IB). L7 was used to create an image plane at the CCD.

As mentioned above, OB was linearly polarized and could be rotated via HP such that it contained both *s*- and *p*-polarization. Because the other writing beam, RB, was *s*-polarized, a degree of *s*-polarization was required in OB to create the required optical interference pattern within the PR device. The *p*-polarized component was necessary to serve as a source for IB. To optimize ϕ, the intensity of IB was monitored as the polarization of OB was rotated and this dependence is illustrated in Fig. 3 (externally applied electric field, $E = 40$ V/μm, AF was removed, and the CCD camera was replaced by a photodiode). Evident in the figure, the intensity of IB was maximized for $\phi = 45°$, and therefore this ϕ was used in all imaging experiments. The intensity of IB was also characterized as a function of E and the result is illustrated in Fig. 4 ($\phi = 45°$). The

maximum intensity of IB occurred at the highest applied field of $E = 70$ V/μm and over-modulation was not observed. Based on these results, $E = 70$ V/μm for all imaging experiments unless otherwise noted.
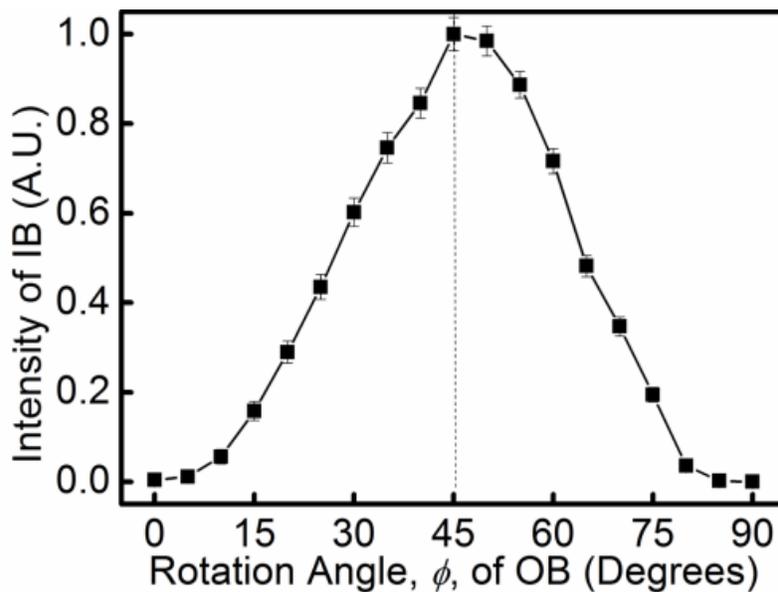

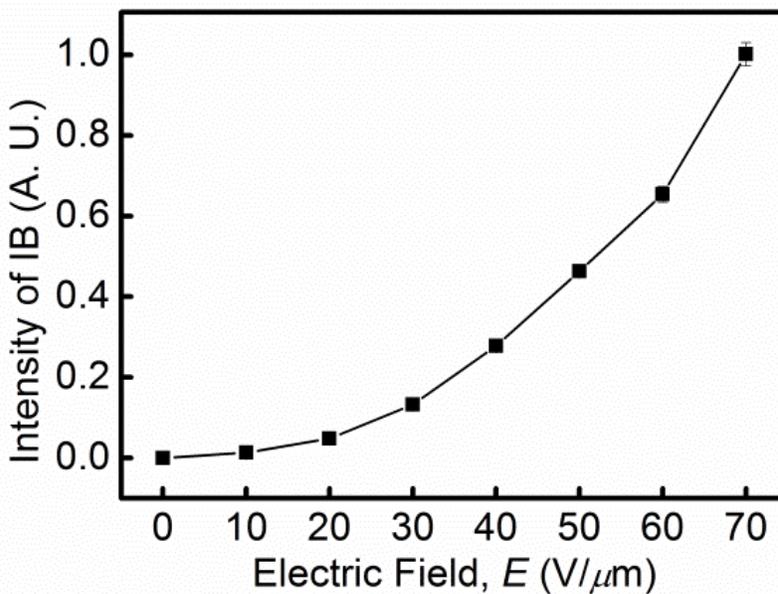**Fig. 3.** Intensity of IB as a function of polarization rotation angle, ϕ, of OB.

Fig. 4. Intensity of IB as a function of external electric field, E.

To gauge the imaging capabilities of the optical system depicted in Fig, 1, an unaberrated image was recorded and is depicted in Fig. 5(A). To obtain this image, the PR device was replaced by a mirror and AB was removed. Evident from the figure, the optical system is capable of producing a clear image. Furthermore, this image serves as a control to which subsequent images can be compared. Removing the mirror and reinserting the PR device, with AB removed, yielded the image depicted in Fig 5(B). In comparing Fig. 5(A) and Fig. 5(B), it is apparent that insertion of the PR device results in a small degree of image degradation. This degradation is attributed primarily to macro- and micro-scale inhomogenialities which likely manifest in the PR composite. To minimize this effect, the PR devices were fabricated with thickness, d, of $d = 50$ μm. This thickness, while relatively thin, ensures the PR grating is in the Raman-Nath regime [9]. An aberrated image depicted in Fig. 5(C) was acquired by replacing the PR device with a mirror and inserting the AB in the position indicated in Fig. 1. As seen in the figure, the image is significantly aberrated. Finally, a corrected image shown in Fig. 5(D) was acquired using all the components depicted in Fig 1. The quality of the corrected image in Fig. 5(D) is nearly identical to the unaberrated image shown in Fig. 5(B), demonstrating the ability to largely eliminate phase aberrations in the optical beam.

The unaberrated RB was obtained using an optical aperture, the position and size of which greatly influenced the ability to restore the image to an unaberrated condition. Reducing the size of the aperture yielded a clearer image, however, at the expense of intensity of IB. It was determined that under the current experimental conditions an aperture diameter of 1 mm yielded an optimal image. For practical applications, the aperture position and size can be adjusted using a feedback system. To demonstrate the
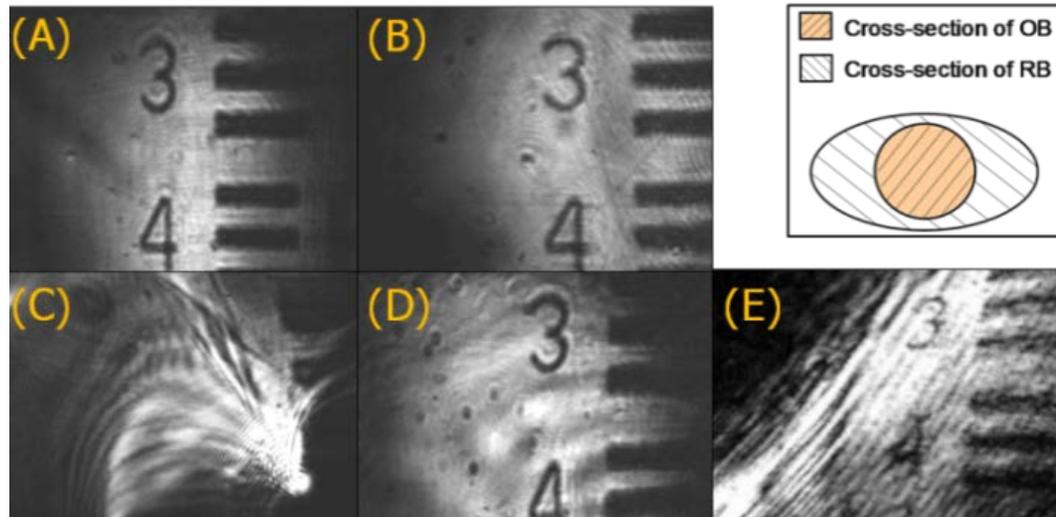
Fig. 5. Images acquired during this study. (A) unaberrated image using a mirror in place of the PR device, (B) unaberrated image captured using the PR device, (C) aberrated image, (D) corrected image, (E) corrected image captured with the optical aperture removed. The inset depicts the configuration of the beam cross-sections of OB and RB at the PR device

necessity of the optical aperture, an image was obtained with the aperture removed and is shown in Fig. 5(E). Apparent from the figure is that the image quality decreased dramatically from that seen in Fig. 5(B). Nevertheless, some degree of correction is observed in comparing Fig. 5(E) to the aberrated image, Fig 5(C). This is attributed to the formation of an effective optical aperture associated with the intersection of OB and RB at the PR device. As illustrated in the inset of Fig. 5, when the optical aperture was removed, the size of RB became larger than that of OB at their intersection at the PR device. Because only the portion of RB which was coincident with OB at the PR device could contribute to the PR grating, those aberrations associated with regions of RB which were not coincident with OB were essentially eliminated. Moreover, the beam cross-section of RB at the PR device was "stretched" horizontally due to the relatively large incident angle of 57.5°, as compared to 22.5° for the OB. Hence, an artificial

aperture was created in the region where interference occurs, effectively reducing the aberrations associated with RB.

The elimination of phase aberrations is rooted in the holographic nature of the PR device. This process is illustrated by Equation (1),

$$|\Psi_{ab} \cdot U_{obj} + U_{ref}|^2$$
$$= U_{obj}^2 + U_{ref}^2 + U_{obj} \cdot \Psi_{ab} \cdot U_{ref}^* + U_{ref} \cdot U_{obj}^* \cdot \Psi_{ab}^*$$
$$= I_{obj} + I_{ref} + U_{ref} \cdot U_{obj}^* \cdot \Psi_{ab}^* + U_{obj} \cdot U_{ref}^* \cdot \Psi_{ab} \tag{1}$$

where U_{OB} and U_{RB} are the amplitudes of OB and RB, respectively, I_{OB} and I_{RB} are the intensities of OB and RB, respectively, U_{OB}^* and U_{RB}^* are the complex conjugates of OB and RB, respectively, and Ψ_{AB} and Ψ_{AB}^* represent the phase aberrations and its complex conjugate, respectively. Here, because an aberrated OB, $\Psi_{AB}U_{OB}$, is used to write the PR grating, and assuming RB is unaberrated, the aberrations are "encoded" in the grating. In a self-induced grating, the PR grating in this case, the grating created by the aberrated OB, $\Psi_{AB}U_{OB}$, is also read by $\Psi_{AB}U_{OB}$. Evident in the last term of Equation (2),

$$\Psi_{ab} \cdot U_{obj} \cdot (I_{obj} + I_{ref} + U_{ref} \cdot U_{obj}^* \cdot \Psi_{ab}^* + U_{obj} \cdot U_{ref}^* \cdot \Psi_{ab})$$
$$= (I_{obj} + I_{ref}) \cdot \Psi_{ab} \cdot U_{obj} + I_{obj} \cdot U_{ref} + (U_{obj} \cdot U_{ref}^* \cdot \Psi_{ab}) \cdot \Psi_{ab} \cdot U_{obj} \tag{2}$$

is that the aberrations, Ψ_{AB}, in the reading OB, $\Psi_{AB}U_{OB}$, and the complex conjugate of the phase aberrations, Ψ_{AB}^*, encoded in the grating, cancel each other so that the optical beam diffracted by the grating, including IB, is aberration-free. A more detailed explanation can be found in literature [15].

The PR composite used in this study was composed of *N,N´*-Bis(3-methylphenyl)-*N,N´*-diphenylbenzidine (TPD), poly(9-vinylcarbazole) (PVK), 4-

homopiperidinobenzylidenemalononitrile (7-DCST) and C_{60} with TPD:PVK:7-DCST:C_{60} = 45:10:45:1.0 wt.%. 7-DCST and C_{60} served as the non-linear optical chromophore and photosensitizer, respectively. A small amount of PVK was included in the composite to enhance its resistance to phase separation, as well as to decrease the dark conductivity. PR composites found in previous studies have often relied on PVK as the charge-transport species [6]. More recently, however, polymers containing TPD pendant functional groups, such as poly(acrylic tetraphenyldiaminobiphenol) (PATPD), have been shown to possess superior functionality [9] [10] [11]. Specifically, the hole mobility of PATPD has been shown to be ∼100 times greater than that of PVK with E = 16 V/μm [10]. A faster charge-carrier mobility is advantageous in PR composites, especially when response time is of concern. In addition, PR devices based on PATPD have shown improved stability in their PR performance [11]. Considering the pendant geometry of the TPD groups in PATPD, it is not surprising that the polymer and the TPD monomer have similar energy gaps, E_{g}, between the highest unoccupied molecular orbital and the lowest occupied molecular orbital, with that of TPD being E_{g} = 3.20 eV and PATPD exhibiting E_{g} = 3.23 eV [12] [13]. Despite the monomeric nature of the TPD used in this study, the PR devices have not exhibited detectable phase separation in over 1 yr. Additionally, due to the predominantly molecular nature of the PR composite, the inclusion of a plasticizer was unnecessary, further increasing the available volume for functional entities within the composite [14]. The PR device was fabricated by melting and sandwiching the composite between two glass slides with coated with indium tin oxide to provide electrodes. The thickness of the PR devices was maintained at d = 50 μm using glass beads.
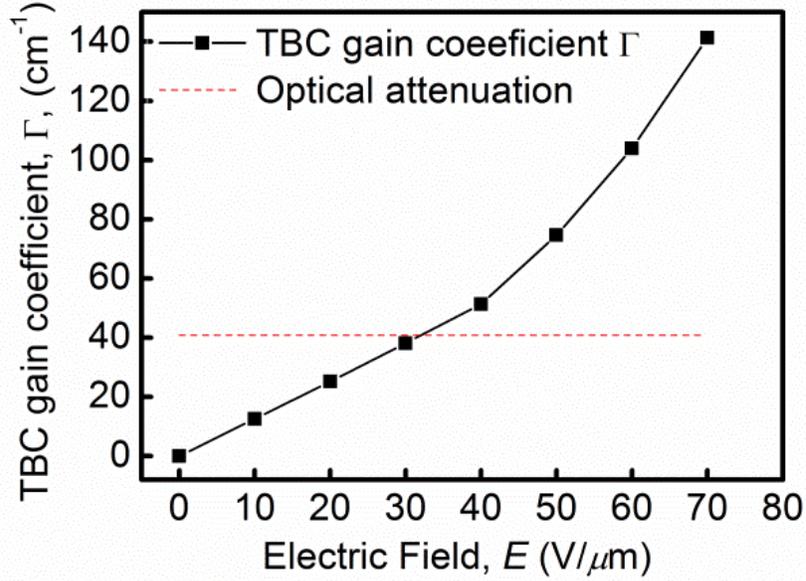
Fig. 6. TBC gain coefficient, Γ, as a function of external electric field, *E*.

To confirm the PR nature of the devices used in this work, two-beam coupling (TBC) techniques were employed using the experimental setup shown in Fig. 1 with minor modifications. Specifically, PBS, AF, AB and HP were removed and OB and RB were *p*-polarized. Bias was applied to the PR device such that RB would experience gain at the expense of OB, and the beam intensity was monitored using a photodiode. The TBC gain coefficients are shown in Fig. 6 as a function of *E* and were calculated according to the equation

$$\Gamma = [ln(\gamma\beta) - ln(\beta + 1 - \gamma)]/L, \qquad (3)$$

where γ is the ratio of the intensity of the beam experiencing gain with and without the pump beam, β is the ratio of the writing beam intensities before the PR device, and L is the optical path length of the beam experiencing gain inside the device. For applications involving TBC-based amplifications, the net gain factor, Γ_{net}, defined as $\Gamma_{net} = \Gamma - \alpha$, should be considered. Here α is the optical attenuation experienced by the beam as it

traverses the PR device, with $\alpha = [\log (I_{RB}'/I_{RB}'')]/d = 40.82$ cm^{-1}, where I_{RB}' and I_{RB}'' are the intensities of RB before and after the PR device, respectively. Evident from Fig. 6, net gain occurs under the current experimental conditions for $E > 40$ V/μm.
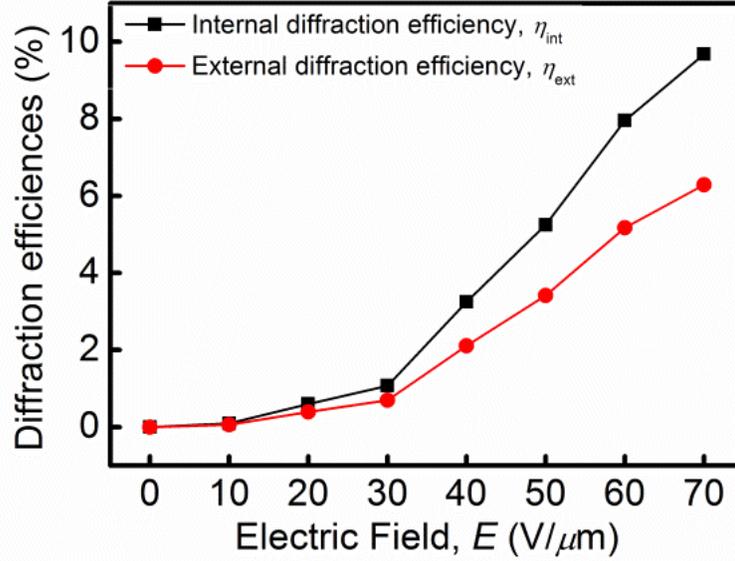

Fig. 7. Diffraction efficiencies, η, as a function of external electric field, E.

To further characterize the utility of the current PR composite for future application in the current optical system, DFWM experiments were performed. As with the TBC experiments, AF, AB, and HP were removed. In this case, OB and RB were s-polarized, and had equal intensities of 12.12 mW/cm^2 at the PR device (adjusted using ND and removing the optical aperture). A p-polarized probe beam with an intensity of 0.06 mW/cm^2 and a beam area of 0.12 cm^2 was made to counter propagate opposite to OB. The diffracted probe beam was collected using a PBS located between L5 and the PR device. The internal and external diffraction efficiencies, η_{int} and η_{ext}, respectively, were measured as a function of E with the results shown in Fig. 7. The efficiencies were calculated using the equations $\eta_{int} = I_d/(I_d+I_t)$ and $\eta_{ext}=I_d/I_p$, in which I_p is the intensity of

the probe beam before the PR device, and I_d and I_t are the intensities of the diffracted and transmitted probe beams, respectively, after the PR device. As seen in the figure, a maximum of $\eta_{int}=$ 10% and $\eta_{ext}=$ 6% were measured at $E =$ 70 V/μm and over-modulation was not observed. While these diffraction efficiencies are relatively low, it is noted that the optical system was optimized for image acquisition. For example, the 40° tilt angle between the PR device normal and the writing beam bisector, while optimized for image reconstruction, dictates that only a small component of E coincides with the grating vector. Also, beam cross-sections were maximized at the PR device in an effort to minimize image distortions. This resulted in beam intensities which were lower than ideal in terms of efficiency. [16, 17].

Time-resolved DFWM experiments were also conducted to characterize the PR grating growth rate, τ_g, under the current experimental conditions. By fitting the obtained data to the Equation

$$\eta(t) = E_{sc}[1\text{-}\exp(\text{-}t/\tau_g)] \tag{4}$$

where E_{sc} is the magnitude of spatial charge field [6], τ_g were determined as 3.53 s, 1.25 s and 0.51 s for $E =$ 50, 60 and 70 V/μm, respectively. To the best of our knowledge this is among the fastest τ_g recorded for any PR device operating in an image correction system [6]. In this case, the improvement in τ_g can likely be attributed largely to the superior charge-carrier mobility of TPD, which allows for faster formation of the space-charge field. The fast τ_g indicates the potential for TPD-based PR composites to be used in applications involving the dynamic processing of optical information.

In summary, a novel optical system employing a TPD-based PR composite for the elimination of phase aberrations is introduced. The optical system has the ability to restore an aberrated, information carrying, optical beam to a nearly unaberrated condition while its potential for application in optical signal transmission is clearly established by the sender-media-receiver geometry. The PR composite shows a net TBC gain for $E > 40$ V/μm, and $\eta_{int} = 6\%$ and $\eta_{ext} = 10\%$ are measured with the current optical system. Moreover, with a $\tau_g = 0.51$ s, the TPD-based PR composite demonstrates potential for real time image correction applications, which is the focus of future research.

ACKNOWLEDGMENT

REFERENCES

1. S. Niu, J. Shen, C. Liang, Y. Zhang and B. Li, Appl. Opt. **50**, 4365 (2011).

2. K. Baskaran, R. Rosen, P. Lewis, P. Unsbo and J. Gustafsson, Optom. Vis. Sci. **89**, 1417 (2012).

3. G. Li, M. Eralp, J. Thomas, S. Tay, A. Schulzgen, R. A. Norwood, and N. Peyghambarian, Appl. Phys. Lett. **86**, 161103 (2005).

4. J. Winiarz and F. Ghebremichael, Appl. Opt. **43**, 3166 (2004).

5. J. Winiarz and F. Ghebremichael, Opt. Express **12**, 2517 (2004).

6. A. Chiou and P. Yeh, Opt. Lett. **10**, 621 (1985).

7. A. Chiou and P. Yeh, Opt. Lett. **11**, 461 (1986).

8. S. Ducharme, J. Scott, R. Twieg, and W. Moerner, Phys. Rev. Lett. **66**, 1846 (1991).

9. S. Köber, M. Salvador, and K. Meerholz, Adv. Mater. **23**, 4725 (2011).

10. K. Ogino, T. Nomura, T. Shichi, S. Park and H. Sato, Chem. Mater. **9**, 2768 (1997).

11. J. Thomas, R. A. Norwood and N. Peyghambarian, J. Mater. Chem. **19**, 7476 (2009).

12. J. Thomas, C. Fuentes-Hernandez, M. Yamamoto, K. Camnack, K. Matsumoto, G. Walker, S. Barlow, B. Kippelen, G. Meredith, S. Marder, and N. Peyghambarian, Adv. Mater. **16**, 2032 (2004).

13. P. K. Nayak, N. Agarwal, N. Periasamy, M. P. Patankar and K. L. Narasimhan, Synth. Met. **160**, 722 (2010).

14. W. Moerner, S. Silence, F. Hache, and G. Bjorklund, J. Opt. Soc. Am. B. **11**, 320 (1994).

15. J. W. Goodman, *Introduction to Fourier Optics*, (McGraw-Hill, San Francisco).

16. K. Meerholz, B. L. Volodin, Sandalphon, B. Kippelen and N. Peyghambarian, Nature **371**, 497 (1994).

17. V. Herrera-Ambriz, J. Maldonado, M. Rodriguez, R. Castro-Beltran, G. Ramos-Ortiz, N. Magana-Vergara, M. Meneses-Nava, O. Barbosa-Garcia, R. Santillan, N. Farfan. F. Dang, P. G. Lacroix and I. Ledoux-Rak, J. Phys. Chem. C. **115**, 23955 (2011).

SECTION

2. CONCLUSION

The work reported in this dissertation demonstrated the recent improvements of TPD-based PR composites in regard to their photosensitization with functionalized semiconductor nanocrystals. Paper III showed a practical application for this type of material in which the optical aberrations can be effectively removed using TPD-based PR composites. This achievement is expected to further enhance the commercialization of PR materials.

VITA

Yichen Liang was born on September 24th, 1987 in Datong, China. He received a Bachelor Degree of Science from Beijing University of Chemical and Technology in 2010, majoring in Polymer Science. In September 2010, he started his PhD education in Missouri University of Sciene and Technology, and joined the Optical Materials Research Group led by Dr. Jeffrey G. Winiarz five months later. His research focuses on organic photoconductive and photorefractive materials and their application in image science. His PhD in chemistry was awarded in May 2016.